**TITLE**

# A CRISPR toolbox for generating intersectional genetic mice for functional, molecular, and anatomical circuit mapping

**AUTHOR NAMES AND AFFILIATIONS**

Savannah J. Lusk[1], Andrew McKinney[1], Patrick J. Hunt[2], Paul G. Fahey[1], Jay Patel[1], Andersen Chang[3], Jenny J. Sun[1], Vena K. Martinez[4], Ping Jun Zhu[1], Jeremy R. Egbert[5], Genevera Allen[6-7], Xiaolong Jiang[1], Benjamin R. Arenkiel[2,8], Andreas S. Tolias[1], Mauro Costa-Mattioli[1], Russell S. Ray[1,8,9]

[1]Department of Neuroscience, Baylor College of Medicine, Houston TX

[2]Department of Molecular and Human Genetics, Baylor College of Medicine, Houston TX

[3]Department of Statistics, Rice University, Houston TX

[4]Department of Pharmacology, Baylor College of Medicine, Houston TX

[5]Department of Cell Biology, University of Connecticut, Farmington CT

[6]Department of Statistics, Computer Science, and Electrical and Computer Engineering, Rice University, Houston TX

[7]Neurological Research Institute, Baylor College of Medicine, Houston TX

[8]McNair Medical Institute, Houston TX

[9]Corresponding author, russell.ray@bcm.edu

## ABSTRACT

### Background

A full understanding of circuits and cellular mechanisms governing health and disease requires the dissection and multi-faceted study of discrete cell subtypes in developing and adult animal models. Recombinase-driven expression of transgenic response alleles represents a significant and powerful approach to delineate cell populations for functional, molecular, and anatomical study. In addition to single recombinase systems, the expression of two recombinases in distinct, but partially overlapping, populations allow for more defined target expression. Although the application of this method is becoming increasingly popular, the expense and difficulty associated with production of customized intersectional mouse lines have limited widespread application to more common allele manipulations that are often commercially produced at great expense.

### Results

We present a simplified CRISPR toolkit for rapid, inexpensive, and facile intersectional allele production. Briefly, we produced 7 intersectional mouse lines using a dual recombinase system, one mouse line with a single recombinase system, and three embryonic stem (ES) cell lines that are designed to study how functional, molecular, and anatomical features relate to each other in building circuits that underlie physiology and behavior. As a proof-of-principle, we applied three of these lines to different neuronal populations for anatomical mapping and functional *in vivo* investigation of respiratory control. We also generated a mouse line with a single recombinase-responsive allele that controls the expression of the calcium sensor Twitch-2B. This mouse line was applied globally to study the effects of follicle stimulating hormone (FSH) and luteinizing hormone (LH) on calcium release in the ovarian follicle.

### Conclusions

Lines presented here are representative examples of outcomes possible with the successful application of our genetic toolkit for the facile development of diverse, modifiable animal models. This toolkit will allow labs to create single or dual recombinase effector lines easily for any cell

population or subpopulation of interest when paired with the appropriate Cre and FLP recombinase mouse lines or viral vectors. We have made our tools and derivative intersectional mouse and ES cell lines openly available for non-commercial use through publicly curated repositories for plasmid DNA, ES cells, and transgenic mouse lines.

**KEY WORDS**

Intersectional genetics, Gene targeting, CRISPR/Cas9, Cre, Flp, Dre, DREADDs, Fluorescent reporter

## BACKGROUND

Targeted expression of effector molecules, like fluorescent markers, calcium reporters, optogenetic actuators, or exogenous ligand-responsive receptors (DREADDs) (1), are increasingly applied in a variety of fields for greater precision, quantitative expression level control, and reduced side effects compared to previous methods for labeling and manipulation. For example, the Cre/LoxP system is used to achieve permanent cell-type restriction by using a promoter or enhancer to express the site-specific recombinase Cre (2). In such examples, Cre transgenes are paired with a constitutively active, but conditional, allele where expression of an effector molecule, such as eGFP, is interrupted by a LoxP-Stop-LoxP cassette that is recombined out by Cre, which enables expression in targeted, Cre-expressing cells. The use of various effector molecules in this paradigm enables fluorescent marking, neuronal perturbation, molecular affinity pull-downs, activity tracking, and other studies (1,3–28).

In many fields, it is becoming increasingly clear that recombinase expression based on a single gene does not offer the resolution needed for a variety of developmental or targeting applications (29–31). Indeed, application of intersectional genetics has led to new progress in various fields including neural circuits, cell type lineage, and embryonic development (32–34). Intersectional genetics adds needed resolution by employing a dual recombinase system using both Cre recombinase as well as a second recombinase, FLP, to activate a conditional effector allele only in cells where both recombinases have been expressed in the same cell (though not necessarily concurrently) (20,35–42). With new methodologies being developed to use Cre and FLP not only as traditional genetic markers, but also as activity and connectivity markers, unique combinatorial cell type definitions become possible (43–47). Thus, a resource consisting of multiple dual recombinase intersectional alleles that each express different effector molecules would add significant value and needed resolution to our ability to deconstruct neural circuits on multiple levels. This technology could also be applied to a multitude of other fields where intersectionally

79 defined subpopulations of target cells exist and may play different roles in the measured
80 outcomes.

81 Although mouse intersectional technology provides relatively benign access to otherwise
82 inaccessible populations of cells, few laboratories have generated single transgenic or
83 intersectional genetic mouse lines in house for several reasons. The complexity and size of the
84 final targeting vectors puts them beyond present (cost-effective) commercial DNA synthesis
85 capabilities, thus requiring some level of recombinant DNA cloning and precluding straightforward
86 production of large, high fidelity ssDNA donors that can facilitate pro-nuclear CRISPR-mediated
87 targeting (48). While intersectional targeting vectors are available from the Addgene plasmid
88 repository, they are finished vectors that require significant reverse engineering or modifications
89 for use in a new context or approach. To our knowledge, there are no modular intersectional
90 targeting vectors that are publicly available for facile and rapid production of new targeting alleles
91 for the generation of intersectional mouse models. Furthermore, vector stability and other *in vitro*
92 difficulties combined with the expense and time associated with target vector insertion and mouse
93 line production limit the number of intersectional mouse lines available for public use. Thus, the
94 production of intersectional genetic mouse lines has been largely limited to a small number of
95 pioneering labs or resource rich institutions such as the Howard Hughes Medical Institute and the
96 Allen Institute for Brain Science (41,49).

97 To address these pitfalls and make the production of intersectional genetic mouse models more
98 widely feasible, we aimed to produce a freely available resource toolbox consisting of several
99 intersectional and single-recombinase responsive *Rosa26* targeting vectors for rapid, facile, and
100 cost-effective generation of complex mouse lines using CRISPR/Cas9-mediated homologous
101 recombination in mouse embryonic stem cells and early oocytes. In oocytes, genomic
102 insertions/deletions (in/dels) and short targeted insertions are readily produced whereas large
103 construct targeting in oocytes has shown more limited but growing success. Additionally, requisite

104 equipment and facilities are difficult to access and out of reach for many investigators. ES cell
105 approaches are well established and widely available, allowing for rapid screening and
106 identification, and, if using morula aggregation, require much simpler methodologies and
107 equipment for mouse generation.

108 Towards this, we produced 7 intersectional mouse lines using a dual recombinase system; one
109 mouse line with a single recombinase system, and three additional ES cell lines to study how
110 functional, molecular, and anatomical features relate to each other in building the circuits that
111 underlie physiology and behavior. As a proof of principle, we applied three of these lines to
112 different neuronal populations for anatomical mapping and functional *in vivo* characterization in
113 respiratory control. Next, we globally applied the single recombinase-responsive line, which
114 controls the expression of the calcium sensor Twitch-2B. Twitch-2B was expressed globally in the
115 generated mouse line to study the effects of follicle stimulating hormone (FSH) and luteinizing
116 hormone (LH) on calcium release in the ovarian follicle. The publication and availability of this
117 technology will allow for the seamless production of a highly diverse group of mouse lines that
118 can be used to generate animal models of human disease, label specific cell populations for
119 developmental or connectivity studies, or modulate cellular activity in established disease model
120 lines, among other possibilities. All reagents and vectors used or generated in this study are now
121 openly available for not-for-profit research.

## RESULTS

**Vector design and optimization:** For each of the targeting vectors generated, the intersectional or Dre-responsive cassette was knocked into a well-established site in the *Rosa26* locus (**Fig. 1)** (50,51). For positive ES cell clone selection, the targeting vector was simplified and improved in several ways compared to earlier approaches (52). A simplified neomycin resistance cassette was integrated into the intersectional cassette before the second LoxP-flanked stop cassette to utilize the *CAG* promoter and polyadenylation (*pA*) sequences of the FRT flanked stop cassette, eliminating prior use of an additional PGK promoter and *Bovine Growth Hormone polyA* (BGHpA*)* signal. To use CRISPR/Cas9, we cloned an sgRNA that was close to the 5'/3' homology junction into the px330 vector (53), which expresses both Cas9 and the subcloned sgRNA (*px330_Rosa26_sgRNA*). A Woodchuck Hepatitis Virus (WHV) Posttranscriptional Regulatory Element (WPRE) and BGHpA were added at the end of the expression cassette to enhance effector molecule expression and limit reliance on the disrupted Rosa Locus for transcript termination (52). The homology arms were significantly shortened to 1Kb to remove repetitive genomic sequences and stabilize the vector for prokaryotic propagation. Lastly, the terminal non-homology Diphtheria Toxin A (DTA) chain negative selection cassette was removed, allowing for the complete targeting vector to be functionally tested via cell culture or *in utero* electroporation, which was not possible with the presence of the terminal DTA selection cassette without an additional subcloning step. Redesigned vectors and their Addgene ID numbers are outlined in Table 1 for public distribution.

**Embryonic stem cell electroporation:** We optimized traditional but widespread ES cell targeting by applying CRISPR/Cas9-mediated HDR (54). Our initial electroporation (EP) experiments using an earlier, more complex version of the *Rosa26* intersectional targeting vector (containing the longer 4.2 kb 3' homology arm, DTA, and no CRISPR/Cas9) showed targeting rates ranging from 6-14% (over the course of four electroporations we saw targeting rates of 6/48, 3/48, 7/48, and

147 3/48 clones, mouse strains listed in **Table 2**). To determine the effect of CRISPR/Cas9 on
148 targeting efficiency, we co-electroporated the *px330_Rosa26_sgRNA* vector expressing Cas9
149 and a *Rosa26* specific sgRNA with the optimized *RR5* targeting vector at four different molar
150 ratios (0:1, 0.5:1, 1:1, and 10:1), proportionally decreasing the amount of donor vector to
151 accommodate the increasing *px330_Rosa26_sgRNA* vector per EP (18-20μg total DNA per EP
152 for $1x10^7$ ES cells) (**Fig 1C)**. Under the 0:1 *px330* vector:donor vector condition, we saw a 6%
153 targeting rate similar to those seen in electroporations without Cas9 and with a much longer 3'
154 homology arm and negative selection, suggesting that the shortening did not have a large impact
155 on targeting efficiency under our EP conditions. Under the 0.5:1, 1:1, and 10:1 conditions, we
156 observed 33%, 27%, and 58% targeting, respectively, suggesting that higher ratios of the Cas9
157 vector resulted in increased targeting efficiency (**Fig. 1D)**.

158 Since the 10:1 ratio had the highest targeting efficiency, despite having significantly less donor
159 DNA, we used this ratio in subsequent EPs. Because the targeting efficiency was notably high,
160 we next attempted a single electroporation with multiple vectors targeting the same locus, but
161 containing equimolar amounts of five different cassettes, while keeping the overall
162 *px330_Rosa26_sgRNA* vector to total donor vector ratio at 10:1. The five vectors consisted of: 1)
163 a Cre/FLP responsive mutant methionyl-tRNA synthetase (*RR6*) for selective labeling of newly
164 synthesized proteins; 2) a Cre/FLP responsive modified G-protein coupled receptor (*RR7*); 3) a
165 Cre/FLP responsive bicistronic reporter with H2B-TagBFP and sfGFP separated by a p2a
166 element, and tdTomato expressed in the subtractive population (cells that express FLP but not
167 Cre) (*RR9*); 4) a Dre-responsive tricistronic reporter with H2B-TagBFP, sfGFP, and
168 synaptophysin-tdTomato separated by p2a elements (*RR11*); and 5) a Dre-responsive bicistronic
169 reporter with H2B-TagBFP and sfGFP separated by a p2a element (*RR10*). We saw a 52%
170 targeting efficiency and successful targeting of all five cassettes at varying efficiencies (**Table 3**).
171 Due to the lower targeting efficiency of *RR7* (2%), we attempted another 10:1 electroporation

172 using the *RR7* donor vector alone and obtained a 63% targeting efficiency (genotyping results
173 shown in **Fig. 1**). Thus, our results show that we are able to target and recover as many as five
174 *Rosa* alleles in a single EP, significantly increasing efficiency and reducing costs toward
175 intersectional mouse generation.

176 **Oocyte targeting:** Given the high efficiency of targeting, we also attempted to create a founder
177 line (*RR8*) through direct oocyte injection of the optimized *Rosa26* targeting vector with a Cre-
178 responsive calcium indicator, Twitch (55) (total cassette size without homology arms, 6.5kb),
179 using pro-nuclear injection of Cas9 protein (30 ng/µl), sgRNA (20 ng/µl), and double-stranded
180 DNA plasmid (2 ng/µl). A total of 1266 embryos were injected yielding 129 mice, of which 7
181 genotyped positive for the calcium indicator but only one targeted successfully (<1% targeting
182 efficiency of mice born), suggesting that direct oocyte injection is inefficient with this system under
183 the specified parameters.

184 **Off-target analysis:** Genomic sequences that are similar to the sgRNA used for targeted double
185 stranded breaks may cause unintended gene mutations or editing at off-target sites. To account
186 for this possibility, we predicted the off-target sites for each sgRNA using the crispr.mit.edu tool
187 and selected the top 5 sites for follow up. We PCR amplified and sequenced these loci from three
188 correctly targeted ES cell clones and did not detect any genetic changes (**Fig. 2**). While we cannot
189 rule out off-target effects in other loci, these data suggest that off-target effects are not prevalent
190 in this setting.

191 **Mouse line derivation:** The goal of our efforts was to produce freely available genetic tools that
192 delineate and access distinct populations for multi-faceted circuit mapping or functional
193 characterization studies. With this toolkit in hand, we collectively produced 11 intersectional or
194 Dre-responsive alleles available as either mouse lines (8) or ES cells (3) **(Table 2)**. To perturb
195 neuron function, we produced three lines that express metabotropic DREADD receptors, hM4D

196 (*RR1*), hM3D (*RR2*), and Rs-EGFP (*RR7*), and a fourth line expressing the ionotropic PSAM
197 receptor (*RR4*) (24,56,57). Two lines enable molecular characterization: one expresses the
198 EGFP-L10A fusion protein for ribosomal affinity purification and capture of translating mRNAs
199 (*RR3*) (58), while the second line expresses methionyl-tRNA synthetase (Met-RS) that
200 incorporates an artificial amino acid into nascent peptides (*RR6*) (13). One line enables ratiometric
201 calcium imaging via expression of Twitch2B (*RR8*). Our neuro-anatomical mapping lines
202 described below also incorporate a tagged histone (H2B), offering the possibility of chromatin
203 affinity isolations. We created four alleles of differing Cre, FLP, and Dre recombinase responsive
204 configurations that fluorescently mark distinct cellular compartments for unambiguous cell counts,
205 morphological characterizations, and projection mapping (*RR5, RR9, RR10, RR11)*. The
206 derivation of lines *RR5*, *RR6*, and *RR7* demonstrated that ES pluripotency was maintained, and
207 that germline transmission was not diminished in our Cas9-mediated single and multiplexed
208 electroporations after correctly targeted clones were selected and injected into blastocysts for
209 chimera generation.

210 **Select mouse line characterization:** Upon dual recombinase expression, the *RR5* tricistronic
211 multi-color reporter allele expresses three spectrally separated and modified fluorescent proteins
212 to highlight the nucleus in blue, fill the neuron in green, and emphasize pre-synaptic contacts in
213 red. At the site of dual recombinase expression, targeted cells are brightly labelled with TagBFP,
214 sfGFP, and tdTomato where TagBFP fluorescence is constrained to the nucleus by an H2B
215 fusion, sfGFP is unmodified so that fluorescence is seen throughout the cell body, and tdTomato
216 is fused to synaptophysin (59) so that fluorescence is excluded from nuclear areas and primarily
217 seen in projection areas. Individual nuclei can be resolved using blue fluorescence and co-
218 localization with sfGFP-labeled somata.

219 We used *RR5* to evaluate the functional activity and specificity *in vivo* of our CRISPR/Cas9
220 approach to generating mouse lines in three distinct contexts; 1) germline recombinase

221 expression, 2) viral recombinase expression, and 3) combinatorial retrograde viral and germline
222 recombinase expression to target single gene defined neurons by a specific projection field. First,
223 to demonstrate genetically-restricted, germline expression of recombinases in the intersectional
224 *RR5* line, we bred the *RR5* line to a double *Dopamine-Beta-Hydroxylase (DBH)*$^{p2aFLPo}$(54); *Bactin-*
225 *Cre* recombinase driver to express the tricistronic fluorescent cassette in *DBH*-positive
226 noradrenergic (NA) neurons in the brainstem **(Fig. 3 A-H, Supplemental Figure 1 A-B)**. In both
227 the locus coeruleus (**Fig. 3 A-D)** and the A5 nucleus (**Fig. 3 E-H)** as well as all other noradrenergic
228 nuclei (not shown), we could cleanly resolve blue nuclei, green cells, and red puncta without the
229 need for antibody enhancement. Additionally, we bred an intersection of double *Vgat-Cre; Vglut2-*
230 *FLPo* recombinase expression to the *RR5* line and found the entopeduncular nucleus labeled
231 green with local projections labeled red and distal projections in the lateral habenula labeled red
232 (DAPI was applied to help delineate the target field, obscuring the genetic TagBFP signal)(60,61)
233 (**Fig. 3 I-P**).

234 Second, we verified viral expression of Cre and FLP recombinase where adult *RR5* mice were
235 stereotaxically injected with equal titer amounts of AAV viruses expressing Cre and FLP (**Fig. 4A,**
236 **Supplemental Figure 1 C**) into the dentate gyrus **(Fig. 4 B-I)**, amygdala (**Fig. 4 J-Q**), and
237 olfactory bulb (**Fig. 4 R-U**). Clear expression of all three fluorescent proteins were resolved at the
238 site of injection to the appropriate cellular locations. Third, defining properties of the
239 subpopulations can be extended to include any combination of gene expression or anatomical
240 location and projection target when injection of retrograde viral vectors is applied. To utilize this
241 option, we genetically marked a neuronal subtype defined by the partial overlap of a genetic
242 selector and projection target by injecting canine adenovirus 2 (CAV2)-Cre virus (62,63) into the
243 basolateral amygdala of *DBH*$^{p2aFLPo}$*; RR5* mice that express only FLP in all noradrenergic neurons.
244 CAV2-Cre virus efficiently transduces axon terminals, thus genetically marking presynaptic
245 neurons. In this context, only noradrenergic neurons expressing DBH that project to the amygdala

246 express both Cre and FLP and the resulting tricistronic fluorescent cassette (**Fig. 5 A)**. We only
247 observed recombination in the brainstem noradrenergic nuclei and in the locus coeruleus,
248 primarily on the ipsilateral side (**Fig. 5 B-E**) with some sparse marking on the contralateral side
249 (**Fig. 5 F-I**), in agreement with a prior study (64). Overlapping red and green puncta (with no blue)
250 could be seen in the injected amygdala, suggesting that the marked neurons project to the
251 amygdala, as expected given the nature of the CAV2-Cre virus (**Fig. 5 J-M).** We also observed
252 collateral projections to several additional areas in the mid and forebrain, including the dorsal
253 raphé (**Fig. 5 N-Q)**, reticulotegmental pontine nuclei **(Fig. 5 R-U)**, dentate gyrus **(Fig. 5 V-Y)**, and
254 olfactory bulb (**Fig. 5 Z-CC).** This restriction by retrograde selection was also achieved in other
255 regions of the brain with a second viral vector. *Vglut2_Cre; RR5* mice were injected with retro-
256 AAV-Ef1a-FLPo into the lateral hypothalamus (**Fig. 6 A**) where tricistronic expression was clearly
257 visualized in the cingulate gyrus (**Fig. 6 B-E**), piriform cortex (**Fig. 6 F-I**), and medial habenula
258 (**Fig. 6 J-M**), indicating these regions as pre-synaptic inputs to the lateral hypothalamus.
259 Together, these results are in agreeance with previous connectivity studies (64).

260 Before *in vivo* characterization of the DREADD systems coded by *RR1* and *RR2*, we first
261 examined the ability of the *RR1 and RR2* lines to modulate dopamine beta-hydroxylase (DBH)-
262 defined noradrenergic neuron activity at the cellular level. We conducted whole-cell recordings
263 from P30-P60 locus coeruleus neurons expressing one of 3 DREADD receptors: hM3D (RR2),
264 hM4D (RR1), or Di (previously published). Each cassette exists with FRT and LoxP bound stop
265 cassettes, so each line was initially bred with Bactin_FLPe to remove the FLP-dependent stop
266 cassette (65). The RC::FrePe was also bred with Bactin_FLPe to remove the FLP-dependent stop
267 cassette and then bred to the cre-only dependent DREADD lines (66). This compound allowed
268 for fluorescent labelling of neurons where Cre recombinase, and thus DREADD receptors, are
269 present. These compounds resulted in mice wherein GFP and a DREADD were expressed in
270 *TgDBH-Cre*-defined cells for acute brain slice visualization (See Supplemental Figure 2 for further

271 genetic details). *RC::PDi* (52) was included as it represents a similarly constructed hM4D
272 intersectional allele, but lacks the modifications and optimizations made in our targeting system
273 (**Fig. 1 A**). For example*, RC::PDi* contains an additional PGK Promoter and pA signal sequence
274 flanking neomycin in the first stop cassette and lacks the WPRE element and pA found in *RR1*
275 and *RR2*. We hypothesized that the addition of a Woodchuck Hepatitis Virus (WHV)
276 Posttranscriptional Regulatory Element (WPRE) would enhance DREADD effectiveness. After
277 bath application of 10 μM CNO, for *RR2P (hM3D); RC::epe* we observed a depolarization of
278 membrane potentials of LC neurons (pre-CNO: -62.26±1.53, post-CNO: -55.09±2.16 mV, paired
279 t-test: p=0.0034, n=19 neurons across 3 mice). After bath application of 10 μM CNO, for *RR1P*
280 *(hM4D); RC::epe* we observed a hyperpolarization of membrane potentials of LC neurons (pre-
281 CNO: -56.98±3.50 mV, post-CNO: -65.3137±3.60 mV, paired t-test: p=0.046, n-10 neurons
282 across 3 mice). After bath application of 10 μM CNO, for *RC::PDi (Di); RC::epe* we observed a
283 hyperpolarization of membrane potentials (pre-CNO: -53.71±2.93 mV, post-CNO: -56.72±3.42
284 mV, paired t-test: p = 0.027, n=10 neurons across 3 mice) (**Fig. 7 A-C**). These data confirmed
285 functional expression of each DREADD system.

286 We next performed whole-body plethysmography to assess changes in respiratory function
287 caused by CNO-DREADD mediated perturbation of targeted neurons *in vivo*. Significant changes
288 in any of the calculated respiratory variables demonstrates a measurable effect of DBH-defined
289 noradrenergic neuronal activity on respiratory control and/ or ventilatory response to $CO_2$. If
290 change was seen in room air, then basal respiratory control was affected by the change in activity
291 of these neurons. If change were seen in 5% $CO_2$, then changes in the activity of these neurons
292 affected the hypercapnic ventilatory response. *DBH-Cre* defined NA neurons were inhibited by
293 crossing mouse line *RR1P* to *Tg(Dbh-cre)KH212Gsat (TgDBH-Cre)* mice. We observed no
294 changes under room air conditions (**Fig. 8 A)**. However, under hypercapnic conditions, we saw a
295 reduction in ventilation (**Fig. 8 B)**, with decreases in $V_T$ (Tidal volume) (-26.6%, p=0.0021, **Fig. 8**

296 **D**), $\dot{V}_E$ (Minute ventilation) (-26.8%, p=0.026, **Fig. 8 E**), and $\dot{V}_E/\dot{V}_{O2}$ (Ventilatory equivalents for
297 oxygen) (-28.7%, p<0.0001, **Fig. 8 G**). No significant differences were observed in body
298 temperature between experimental animals and sibling controls (**Fig. 8 H**). Notably, sibling
299 controls showed no difference in respiratory parameters pre- and post-CNO administration.

300 We then tested the applicability of the *RR2P* line *in vivo.* After CNO-DREADD mediated
301 stimulation of *DBH-Cre* defined neurons, we saw significant increases under room air ventilation
302 (**Fig. 9 A)** in $V_f$ (Ventilatory frequency) (+28.1%, p=0.0076, **Fig. 9 C**), $V_T$ (+43.3%, p=0.00077,
303 **Fig. 9 D**), $\dot{V}_E$ (+83.6%, p<0.0001, **Fig. 9 E**), and $\dot{V}_{O2}$ (Oxygen consumption) (+50.9%, p<0.0001,
304 **Fig. 9 F**). The increase in $\dot{V}_E$ was proportional to the increase in $\dot{V}_{O2}$, however, so $\dot{V}_E/\dot{V}_{O2}$ did not
305 change **(Fig. 9 G)**. Under hypercapnic conditions, as compared to pre-CNO values, $\dot{V}_{O2}$ was
306 increased (+37.2%, p=0.0015, **Fig. 9 F)**, resulting in a reduced $\dot{V}_E/\dot{V}_{O2}$ (-24.2%, p=0.04, **Fig. 9 G)**.
307 We also observed a deficit in body temperature in *DBH-Cre; RR2P* animals 30 minutes after the
308 end of the assay at room temperature (~1.5 hrs after CNO injection) as compared to sibling
309 controls (**Fig. 9 H)**, but not immediately at exit from the respiratory chamber, which is kept at a
310 thermoneutral temperature, 30-32°C**.** Sibling controls showed no difference in respiratory
311 parameters pre- or post-CNO administration. The respiratory phenotypes seen here clearly
312 demonstrate an acute and cell autonomous involvement of the whole NA system in $CO_2$
313 chemosensitivity and baseline metabolism while avoiding the confounds of developmental
314 compensatory events or off-target effects.

315 Finally, we characterized a fourth line, produced by oocyte CRISPR-mediated recombination to
316 express the Twitch2B ratiometric calcium indicator upon Cre recombinase expression. Calcium
317 signaling was recorded in outer granulosa cells surrounding an oocyte taken from a germline
318 recombined (*RR8; Bact_Cre*) mouse line (**Fig. 10 A**). Upon application of 10μM ionomycin in the
319 presence of 10mM $CaCl_2$, the YFP/CFP ratio increased more than 3-fold (**Fig. 10 B**). The data

320 demonstrate how the targeting system here can be used to build conditional mouse lines that are
321 useful beyond the nervous system and throughout the body (67).

322 Collectively, these data highlight how our single recombinase and intersectional lines can be used
323 to functionally assess dispersed and difficult to access populations, setting the stage for further
324 characterization and dissection of a variety of systems in a given measured outcome through
325 intersectional subdivision by genetic or viral methods.

326 **DISCUSSION**

327 **Vector design and optimization:** Our tricistronic mouse line vector (*RR5*) was a complex vector
328 to design. Thus, the discussion of its construction applies to the other simpler vectors and best
329 describes choices made to optimize the vectors. Our initial goal was to create an intersectional
330 mouse strain expressing three fluorescent components to highlight the nucleus, whole neuron,
331 and presynaptic contacts, enabling facile study of cell counts, cellular morphology, and axonal
332 and projection targets (*RR5* consisting of H2B-TagBFP, sfGFP, and synaptophysin-tdTomato
333 separated by p2a elements) without the need for signal amplification using antibodies. However,
334 likely due to the high number of repetitive elements in the *Rosa26* 3' homology arm and the high
335 complexity and repetitive components of the intersectional cassette (i.e. two stop cassettes
336 consisting of multiple SV40 polyadenylation sequences, tdTomato protein dimer, double loxP and
337 FRT sites, and two p2a self-cleaving peptides separating the elements), we had no success in
338 stably subcloning the intersectional cassette into a low copy vector (p15a ori) containing the
339 original *Rosa26* homology arms (1.1kb 5' homology arm and 4.2 kb 3' homology arm) and DTA
340 negative selection gene (52). Thus, we sought to make several improvements on the prior
341 approaches used to build intersectional genetic mice. First, we sought to stabilize the vector by
342 shortening the homology arms and eliminating repetitive genomic elements found at the *Rosa26*
343 locus. Second, we removed the DTA negative selection terminal non-homology to eliminate the
344 need to validate intersectional cassettes separately before placing the cassette in the targeting
345 vector. Third, we reduced the size of the selection cassette. Prior intersectional constructs carried
346 an additional PGK promoter and BGHpA tail for neomycin expression. We eliminated both
347 promoter and BGHpA as the functions of these elements can easily be served by the CAG
348 promoter and SV40pA in the stop cassette. With smaller homology arms, it was possible that our
349 targeting efficiency would fall. Therefore, we introduced a CRISPR/Cas9 targeting strategy to
350 enhance homologous recombination in either ES cells or oocytes. Surprisingly, in ES cells, the

351 shorter homology arms performed equally well as the full-length homology arms (see discussion
352 below). The resulting strategy offered a simplified, smaller, and highly stable vector that remains
353 efficient at targeting the *Rosa26* locus. Through this optimization process we built a set of baseline
354 vectors that can be used to build any intersectional genetic targeting allele rapidly and
355 inexpensively by simply cloning in a cDNA of interest into one or both of the multiple cloning sites
356 for both intersectional and subtractive expression.

357 **Embryonic stem cell electroporation:** While CRISPR strategies are widespread for knockout
358 mutations and small deletions and insertions in mouse zygotes, consistent knock-in of large
359 targeting cassettes (>4kb) still remains a challenge with fewer but increasing successes (68–70).
360 To address this limitation, our new multiplexed methodology enabled us to: **1)** simplify our base
361 targeting vector to less than 5kb in total length; **2)** see successful targeting of added cassettes up
362 to 11kb; **3)** increase the rate of targeting by 5-10 fold over previous *Rosa26* targeting attempts
363 (that used a significantly longer 3' homology arm) under our ES cell strain and conditions; and **4)**
364 further reduce cost by co-electroporating five different targeting vectors in a single ES cell
365 electroporation that were easily resolved to produce new mouse lines. While targeting rates for
366 the *Rosa26* locus can vary greatly in the literature, we compare only to our own experiments, as
367 significant variability in targeting efficiency from lab to lab or facility to facility can arise from the
368 several factors in ES cell electroporation ranging from electroporation conditions (e.g. buffer ionic
369 strength, adjuvants, field strength, field duration, field shape, square wave vs exponential decay,
370 etc.) to culture conditions (ES cell strain and genetic background, feeder type, media composition,
371 inclusion of LIF, etc.). Notably, when we co-electroporated a CRISPR/Cas9 plasmid to facilitate
372 targeting, there was a proportional increase in targeting efficiency despite reduced amounts of
373 targeting vector (total DNA in the EP was capped at 18-20 µg per EP). At the highest efficiencies,
374 we could further subdivide the small amount of targeting vector across multiple plasmids, which
375 allowed us to introduce and recover as many as five vectors in a single EP. This multiplexed

376 approach significantly reduced the costs of mouse production via ES cells. With these goals met,
377 multiplexed ES cell targeting enables the rapid and high throughput production of intersectional
378 alleles that can be readily distributed throughout the mouse research community for further
379 studies.

380 **Oocyte targeting:** Oocyte injection was only attempted with one line, *RR8*. Less than 1% of the
381 embryos contained a properly targeted vector, which in our experience suggests that direct oocyte
382 injection is not efficient. Future optimization and the development of new technologies may
383 increase the efficiency of targeting for more rapid generation of transgenic mice; for example, a
384 study showed 10-20% targeting of 8-11kb cassettes to the *Rosa26* locus in oocytes using longer
385 homology arms, while another showed successful targeting of a 5.5kb cassette into the *Rosa26*
386 locus in rats with co-injection of two ssDNA oligos (70,71). As noted above, there can be
387 significant variability in targeting across labs based upon a variety of factors including background
388 strain (vs strain from which the homology arms are derived), the use of Cas9 mRNA or protein,
389 and site of injection (pro-nucleus vs cytoplasm, single vs 2-cell stage). Thus, our outcomes here
390 may reflect our core facility capabilities as much as inherent limitations in consistent Cas9
391 mediated oocyte targeting of large constructs. The successful outcomes here and in a prior
392 publication demonstrate the use of the system to develop lines capable of functional imaging (67).

393 **Select mouse line characterization:** Intersectional expression of fluorescent proteins (FPs) has
394 been used to great effect for anatomical characterizations of targeted neuron populations (66,72).
395 Characterizations aimed at counting or highlighting single cells or cell populations made with a
396 single FP can be made difficult, however, in cases where cell, axon, or dendrite density (neuropil)
397 is high. Usually, one or two FPs are deployed to either fill the cell or highlight specific features,
398 which necessitates the use of multiple reporter alleles to clearly observe cell number, morphology,
399 and projections. To ameliorate these issues, we sought to create a mouse line (*RR5*) that
400 highlights three specific features in an intersectionally defined neuron. Overall, this novel three-

401 color mouse line enables intersectional and simultaneous labeling of three subcellular
402 compartments. The polycistronic fluorescent labeling cassette gives unambiguous cell counts and
403 clear visualization of cell morphology, axonal projections, and synaptic contacts. The strength of
404 expression of all three colors is likely due to the use of p2a elements, rather than IRES elements,
405 which cause expression level reduction. Reduced expression from an IRES may stem from cryptic
406 splice elements in the IRES that could interact with the intron in the CAG promoter or splice
407 acceptors in some stop cassettes (73). Our use of P2A appears to bypass those issues as all
408 three fluorescent proteins could be readily visualized without additional enhancement as
409 compared to other approaches (38).

410 We also show that combinations of germline, viral, and retrograde viral expression of
411 recombinases in the *RR5* line can all be used to clearly map the shared innervation of multiple
412 regions by a small subset of genetic, projection, and/ or intersectionally defined neurons. In
413 contrast to prior intersectional studies using two genetic delimiters to define a subpopulation with
414 a single fluorescent protein (with or without an inert retrograde marker injected into separate sites
415 in the brain), our approach enables facile collateral mapping across the whole nervous system
416 with higher resolution that is growing in popularity (36,64,72). These results demonstrate that
417 despite the high complexity and repetitive nature of the *RR5* cassette, we could efficiently target
418 this allele, the allele remains stable through germline transmission, and it is responsive to Cre
419 and FLP recombinase expression. The restriction of expression to anatomically defined NA
420 neurons as a whole or as a projection subset further establishes the recombinase specificity of
421 our targeting schematic. This approach should also translate equally well to further anatomical,
422 functional, and molecular characterizations of NA and other subtypes defined by their projection
423 patterns with the use of the additional lines reported here.

424 The outcomes of either inhibiting (*RR1P; TgDBH_Cre*) or stimulating (*RR2P; TgDBH_Cre*) NA
425 neurons as defined by *TgDBH_Cre* strongly support the functionality of these two lines in an *in*

426 *vivo* setting. Noradrenergic (NA) neurons are strongly implicated in control of respiratory
427 homeostasis and chemosensitivity (8,74–80). Previous studies focused on demonstrating the role
428 of NA neurons in breathing bear methodological caveats such as lack of resolution due to overly
429 broad lesions or injections (81), developmental and non-cell-autonomous compensation after
430 gene mutations, restraint or anesthesia *in vivo*, and they typically lack concurrent metabolic
431 measurements ($\dot{V}_E/\dot{V}_{O2}$) (82), thus direct comparisons are difficult. Nonetheless, previous work
432 has been reiterated in many ways with our results here in that focal pharmacological NA lesions
433 decreases respiratory frequency and hypercapnic ventilatory response (76). Here we show in
434 conscious, unrestrained mice that inhibition of *TgDBH_Cre*-defined noradrenergic neurons led to
435 significantly reduced tidal volume, minute ventilation, and $\dot{V}_E/\dot{V}_{O2}$ following hypercapnic exposure.
436 On the other hand, activation of *TgDBH_Cre*-defined noradrenergic neurons led to significantly
437 increased respiratory rate, tidal volume, minute ventilation, $\dot{V}_{O2}$, and $\dot{V}_E/\dot{V}_{O2}$ in the room air
438 breathing condition. These changes likely stem from a combined increase in central and
439 peripheral (sympathetic) outflow increasing overall metabolic rate ($\dot{V}_{O2}$). Although breathing and
440 $\dot{V}_{O2}$ are both increased, a small but significant mismatch occurs in hypercapnia suggesting that
441 global excitation may destabilize hypercapnic reflexes as well. Notably, after removal from the
442 thermo-neutral recording chamber, the body temperature dropped significantly. This drop is
443 consistent with prior studies that show central NA outflow to the hypothalamus negatively
444 regulates body temperature (83,84). The magnitude of changes seen for both stimulation and
445 inhibition of *TgDBH_Cre* defined NA neurons in various breathing parameters, particularly for
446 hypercapnia, is in line with expectations of a highly redundant chemosensory system in the
447 respiratory network along with the fact that the NA system is neuromodulatory in nature
448 (37,52,85–88). Altogether, the numerous breathing, metabolic, and temperature changes
449 observed support the functionality of these lines for *in-vivo* chemogenetic manipulations. These
450 data represent modulation of the noradrenergic system that, methodologically, significantly

451 deviates from previously published studies interrogating this system and provides an alternative
452 to those investigating control of breathing that reduces the influence of unintended effects.

453 In conclusion, the methods presented here represent a significant improvement in feasibility and
454 affordability for labs to generate their own intersectional mouse models for application in a variety
455 of fields. Our vector design and application allow for large cassettes to be targeted to the *Rosa26*
456 locus with high throughput, increased efficiency, germline transmission, and preserved
457 pluripotency. These protocols and techniques can be used to investigate most, if not all, neural
458 circuits in the context of development and/ or disease. Implementing these techniques also serves
459 as an alternative to cost-prohibitive commercially available vectors and mouse lines. Together,
460 we present a facile, cost-effective method for producing gene specific intersectional mouse lines.

461 **CONCLUSIONS**

462 During development, many distinct cellular subtypes arise and intercalate to create the complex
463 cells, organs, and organ systems that constitute our behavior and physiology. Key to
464 understanding this organization and how it may be perturbed in diseases is the ability to identify
465 and access discrete cell subtypes in the developing and adult mouse for multi-faceted studies. It
466 is now clear that even within narrowly defined cell types once thought as homogeneous,
467 significant diversity is found at multiple levels including genetic and molecular signatures, activity
468 patterns, synaptic connectivity, and projection patterns. Given this complexity, it is often difficult
469 to define and access specific cellular populations for study, particularly during embryogenesis,
470 where *in utero* development makes access problematic. In neuroscience, the power of studying
471 combinatorially defined neuronal populations increases significantly when multiple distinct
472 neuronal features, such as birthdate, collateral projection targets, molecular profiles, or a
473 functional requirement in a given physiological process or behavior can be examined in parallel
474 to reveal deeper insights into the mechanisms involved in the establishment and maintenance of
475 neural circuit organization. However, the ability to carry out such studies is restricted by the limited
476 number of publicly available intersectional mouse lines as well as the inherent difficulty in
477 developing new intersectional alleles.

478 We present a novel CRISPR/Cas9-mediated system for consistently targeting large cassettes to
479 the *Rosa26* locus for high throughput and parallel generation of intersectional and conditional
480 mouse lines. These studies demonstrate that CRISPR/Cas9 can be used to increase targeting
481 efficiency at the *Rosa26* locus in mouse embryonic stem cells with shortened 1-1.2 kb homology
482 arms while preserving pluripotency and the ability to transmit alleles via the germline. This
483 technology allows for the opportunity to generate mouse lines that express a wide range of
484 effector molecules in various cell types, enabling the developmental, anatomical, molecular, and
485 functional characterization of cellular organization in behavior and physiology. To democratize the

generation of intersectional and conditional targeted ES cells and mouse lines, we have generated a publicly available vector toolkit for single-step cloning into *Rosa26*-targeting vectors for double and single-recombinase responsive cassettes (**Table 1).** We have also generated several mouse lines available, without restriction, to the not-for-profit research community enabling high specificity intersectional access of neuronal and other populations for cross correlative mapping approaches using functional neuronal perturbation, molecular profiling, and anatomical characterizations for multifaceted studies (**Table 2**). Overall, these resources and the modular nature of the intersectional approach make rapid and low-cost production of large numbers of intersectional alleles possible that can be efficiently distributed as ES cells or mouse lines throughout the mouse research community. All vectors (Addgene; 97007-97012, 99142), mouse lines (MMRRC; 043513-043519), and ES cells (BCM ES Cell Core Facility) have been made publicly and unconditionally available to the academic research community.

498 **METHODS**

499 **Construction of targeting and Cas9 vectors**: The simplified *Rosa26* targeting vector was
500 derived using standard cloning procedures from a targeting vector used in previous studies (52)
501 consisting of a p15a origin of replication, kanamycin selection cassette, DTA negative selection
502 cassette, and *Rosa26* homology (1081 bp 5' homology arm and 4342 bp 3' homology arm). The
503 total vector size was 9084 bps. The DTA was removed and the 5' homology arm was shortened
504 to 1025 bp fragment (deleting the sgRNA target sequence (chr6:113,076,062-113,077,087
505 GRCm38/mm10)) while the 3' homology arm was shortened to 1231 bps (chr6:113,074,801-
506 113,076,032 GRCm38/mm10), maintaining the insertion site within the first intron and reducing
507 the total vector length to 4694 bps and eliminating a number of repetitive regions that often
508 resulted in vector instability when constructing intersectional targeting vectors.

509 For the Cas9 expressing vector, we selected an sgRNA target sequence that was close to the 5'
510 and 3' junction of the *Rosa26* gene locus (ACTGGAGTTGCAGATCACGA with PAM motif GGG;
511 chr6:113,076,040-113,076,05 GRCm38/mm10). The selected sgRNA was cloned into the BbsI
512 sites of the px330 vector that expresses Cas9 (final vector is called *px330_Rosa26_sgRNA*).

513 Knock-in cassettes were assembled in either 1) a previously used intersectional template plasmid
514 (*RR1-4, RR6-7*); 2) a newly constructed intersectional template plasmid with neomycin promoter
515 and pA elements removed (*RR5* and *RR8*); or 3) a constructed Dre-responsive template plasmid
516 (*RR9* and *RR10*). The intersectional plasmid consisted of a ubiquitous *CAG* promoter sequence;
517 an *FRT*-flanked stop cassette consisting of a PGK-neo sequence (for positive selection of
518 targeted ES cells) and three *SV40 pA* sequences; a *LoxP*-flanked stop cassette containing
519 mCherry and a PBS302 stop cassette; and a cloning site for insertion followed by a *WPRE* and
520 *BGHpA* sequence. The new intersectional template consisted of a ubiquitous *CAG* promoter
521 sequence; an *FRT* flanked stop cassette consisting of a neomycin sequence and *His3_SV40 pA*;

522 a *LoxP*-flanked subtractive cloning site stop cassette consisting of a *His3_SV40 pA*; and a cloning
523 site for insertion followed by *WPRE* and *BGHpA* sequences. The Dre-responsive template
524 consisted of a *Rox*-flanked stop cassette consisting of a neomycin sequence and PBS302 stop
525 cassette, and a cloning site followed by a *WPRE* and *BGHpA* sequence.

526 For assembly of complete targeting vectors, the cDNAs of interest were PCR amplified and cloned
527 into the corresponding vector. The intersectional or Dre-responsive cassettes were then cut out
528 with PacI or PacI/AscI and cloned into the shortened *Rosa26* targeting vector.

529 To facilitate single step cloning of complete targeting vectors, we generated a vector toolkit (**Table**
530 **1)** by constructing and moving empty *CAG* cassettes in the Rosa26 targeting vector. We
531 generated four template vectors with neomycin resistance: 1) a Cre/FLP responsive targeting
532 vector; 2) Cre only; 3) FLP only; and 4) Dre-responsive targeting vector. The intersectional
533 template vector consists of the *CAG* promoter, an *FRT*-flanked neomycin resistance gene and
534 stop cassette, a subtractive cloning site (EcoRV) and stop cassette flanked by *LoxP* sites, an
535 intersectional cloning site (PmeI), and *WPRE* and *BHGpA* elements. Each single template vector
536 consists of the *CAG* promoter, stop cassette(s) and neomycin resistance cassette flanked by
537 recombinase sites, cloning site (SwaI), and *WPRE* and *bgh polyA* elements. Additionally, for
538 possible direct oocyte injections we also generated a Cre/FLP responsive targeting vector that
539 does not contain a neomycin resistance gene, with a subtractive cloning site (EcoRV) and
540 intersectional cloning site (SwaI). All cloning sites are blunt restriction enzyme sites for cloning
541 facilitation.

542 Sequences of the template vectors and *px330* vector and plasmids are available through Addgene
543 (provisional ID #s 97007-97012, 99142).

544 **Generation of knock-in mice:** Embryonic stem (ES) cells (AB2.2) were electroporated with 15-
545 20 µg of varying ratios of the *px330_Rosa26_sgRNA* vector to the targeting vector. Neomycin

546 selected clones were screened for homologous recombination using PCR genotyping. Targeted
547 clones were identified using PCR genotyping for 5' and 3' targeting from outside the homology
548 arm and were considered to be successful targeting events if positive for both 5' and 3'
549 genotyping. We used pairs 5'CGCCTAAAGAAGAGGCTGTG (Rosa26-F) and
550 5'GGGCGTACTTGGCATATGAT (CAG-R), producing a 1450 bp band; and
551 5'AATCAACCTCTGGATTACAAAATTT (WPRE-F) and 5'TGGCTCCTCTGTCCACAGTT
552 (Rosa26-R), producing a 2472 bp band.

553 Select targeted clones were microinjected into C57B1/J6 blastocysts and chimeric males were
554 bred to wildtype C57B1/J6 females to achieve germline transmission.

555 **Pronuclear injection**: We constructed a targeting vector by cloning a calcium indicator, Twitch-
556 2B (55), into the Cre responsive *Rosa26* targeting vector. The Baylor College of Medicine
557 Embryonic Stem (ES) Cell Core generated the *Rosa26*-specific sgRNA and Cas9 protein for
558 injection. Pronuclear injections were performed by the Baylor College of Medicine Genetically
559 Engineered Mouse (GEM) Core using the following parameters: 30 ng/µl Cas9 protein, 20 ng/µl
560 sgRNA, and 2 ng/µl dsDNA plasmid. Potential founders were screened for targeting as described
561 above.

562 **Breeding, genetic background, and maintenance of mice**: We maintained colonies of select
563 mouse strains by backcrossing to C57BL/6J mice. For routine genotyping, we carried out PCR
564 amplification of DNA from ear punch preparations using the boiling alkaline lysis procedure.
565 *Rosa26* specific primers for the mice were 5'-GCACTTGCTCTCCCAAAGTC, 5'-
566 GGGCGTACTTGGCATATGAT, and 5'-CTTTAAGCCTGCCCAGAAGA, and yield a 495 bp band
567 (targeted) and 330 bp band (wt). For histology experiments, *RR5* mice were bred to
568 *DBH*$^{p2aFLPo}$(54)*; B6N.FVB-Tmem163*$^{Tg(ACTB\text{-}cre)2Mrt}$*/CjDswJ (Bactin-Cre)* and *DBH*$^{p2aFLPo}$ mice. For
569 plethysmography experiments, *B6.FVB(Cg)-Tg(Dbh-Cre)KH212Gsat/Mmucd (DBH-Cre)* mice

570 were mated with homozygous Cre-only responsive *RR1P* and *RR2P* mice (after crossing
571 intersectional alleles to *B6;SJL-Tg(ACTFLPe)9205Dym/J* [JAX 003800] mice to recombine out
572 the FLP-responsive stop cassette followed by homozygosity) to derive animals in which all mice
573 carried the Cre-responsive hM4D or hM3D allele. Sibling animals that did not inherit the *Cre* allele
574 were used as control animals to the *Cre* positive offspring. For electrophysiology experiments,
575 *DBH-Cre; RR2P* mice were mated to *RC::ePe* mice expressing a floxed eGFP. Cre-specific
576 primers were 5'-ATCGCCATCTTCCAGCAGGCGCACCATTGCCC and 5'-
577 GCATTTCTGGGGATTGCTTA and yielded a 550 bp band if positive. FLPo-specific primers were
578 5'CACGCCCAGGTACTTGTTCT and 5'CCACAGCAAGAAGATGCTGA and yielded a 226 bp
579 band if positive.

580 Established mouse lines reside at the Mutant Mouse Regional Resource Center (MMRRC) and
581 will be unconditionally available to the academic research community (MMRRC 043513-043519).
582 Targeted ES cells have been archived and are available upon request under the condition that
583 any new mouse lines are deposited in a public repository.

584 All animal experiments were performed with the approval of IACUC.

585 **Off-target analysis**: Off-target sequences were identified using the Optimized CRISPR Design
586 tool (crispr.mit.edu). The top 5 sequences for each sgRNA were amplified from selected targeted
587 ES cells and sequenced to determine if any mutations or changes occurred in off-target sites.

588 **Viral injection**: To test the functionality of the *RR5* mouse strain, adult *RR5* mice were injected
589 with equal titers of AAV9-hSyn-FLPo and AAV1-hSyn-Cre viruses (obtained from M. Xue at BCM,
590 250 nl at $1.12 \times 10^{12}$ GC/mL) into the dentate gyrus (coordinates from bregma AP=-2.70, DV=-
591 2.12, ML=1.84) and with equal titers of AAV-EF1a-Cre-WPRE and AAV-EF1a-FLPo-WPRE (UNC
592 Vector Core, 250 nl at $5.06 \times 10^{11}$ GC/mL) into the amygdala (coordinates from bregma AP=-1.06,
593 DV=-4.61, ML=-2.86) and allowed to incubate for 7-14 days. For expression in the olfactory bulb,

594 adult *RR5* mice were injected with AAV-CAG-Cre (obtained from Neuroconnectivity Core at Jan
595 and Dan Duncan Neurological Research Institute, AAV2/9 690 μL at $5.37 \times 10^{13}$ pp/mL) and AAV-
596 Ef1a-Flp (obtained from Neuroconnectivity Core at Jan and Dan Duncan Neurological Research
597 Institute, AAV2/9 690 μL at $7.16 \times 10^{11}$ pp/mL) into the core of the olfactory bulb (coordinates from
598 bregma AP=4.5mm, DV=-2.25mm, ML=±0.8mm) and allowed to incubate for 14 days. For the
599 CAV2-Cre virus experiments, *RR5; DBH$^{p2aFLP}$* mice were injected with CAV2-Cre virus (IGMM
600 Viral Core, 500 nL at $6.0 \times 10^{12}$ pp/mL) into the amygdala (coordinates -2.86, -1.06, -4.61) and
601 allowed to incubate for 17 days. For the Retro-AAV-Ef1a-FLPo virus experiments, *RR5;*
602 *Vglut2_Cre* mice were injected with Retro-FLPo virus (obtained from Neuroconnectivity Core at
603 Jan and Dan Duncan Neurological Research Institute, 690 μL at $1.49 \times 10^{12}$ pp/mL) into the lateral
604 hypothalamic area (coordinates from bregma AP=-1.22mm, DV=-5.12mm, ML=±0.97mm) and
605 allowed to incubate for 21 days.

606 **Histology**: For *RR5* expression, animals were sacrificed and transcardially perfused with 0.1M
607 phosphate-buffered saline (PBS) then with 4% paraformaldehyde (PFA) in PBS. Brains were
608 dissected out and drop fixed for two hours in 4% PFA before a PBS rinse and equilibration in 20%
609 sucrose in PBS. Brains were sectioned into 30-40 μm coronal sections and mounted on slides.
610 Images were collected on a Zeiss confocal LSM780 microscope or Leica TCS SPE confocal
611 microscope.

612 **Electrophysiology**

613 ***Slice preparation***

614 Slice preparation from the mouse LC follows an N-Methyl-D-glucamine (NMDG) slicing protocol
615 (89,90). Briefly, animals were deeply anesthetized using 3% isoflurane. After decapitation, the
616 brain was removed and placed into cold (0−4 °C) oxygenated NMDG solution containing 93 mM
617 NMDG, 93 mM HCl, 2.5 mM KCl, 1.2 mM $NaH_2PO_4$, 30 mM $NaHCO_3$, 20 mM HEPES, 25 mM

618 glucose, 5 mM sodium ascorbate, 2 mM Thiourea, 3 mM sodium pyruvate, 10mM $MgSO_4$ and 0.5
619 mM $CaCl_2$, pH 7.35 (all from SIGMA-ALDRICH). Horizontal slices were prepared using a
620 vibratome (200 µm thick) using zirconia blades. The brain slices were kept at 37.0 ± 0.5 °C in
621 oxygenated NMDG solution for 10 minutes. They were then transferred to an artificial
622 cerebrospinal fluid (ACSF) containing 125 mM NaCl, 2.5 mM KCl, 1.25 mM $NaH_2PO_4$, 25 mM
623 $NaHCO_3$, 1 mM $MgCl_2$, 25 mM glucose, and 2 mM $CaCl_2$ (pH 7.4) for at least 1 hour prior to the
624 beginning of recordings. During the recording sessions, the slices were submerged in a
625 commercially available chamber (Luig Neumann, Order No. 200-100 500 0150-M) and were
626 stabilized with a fine nylon net attached to a custom-designed platinum ring. This recording
627 chamber was continuously perfused with oxygenated physiological solution throughout the
628 recording session.

629 ***Recordings***

630 Whole-cell recordings were performed as described previously (90–92). Briefly, patch pipettes (2-
631 7 MΩ) were filled with an internal solution containing 120 mM potassium gluconate, 10 mM
632 HEPES, 4 mM KCl, 4 mM MgATP, 0.3 mM $Na_3GTP$, 10 mM sodium phosphocreatine and 0.5%
633 biocytin (pH 7.25). Whole-cell recordings from up to 8 LC neurons were performed using two
634 Quadro EPC 10 amplifiers (HEKA Electronic, Germany). PatchMaster (HEKA) and custom-written
635 Matlab-based programs (Mathworks) were used to operate the recording system and perform
636 online and offline data analysis. In current-clamp recordings, neurons were first current clamped
637 at ~-40pA to prevent spontaneous firing. Prior to investigating the effect of drugs, we calculated
638 spike thresholds and recorded firing patterns in response to sustained depolarizing currents by
639 injecting increasing current steps (+10pA). Continuous recordings were obtained from LC neurons
640 current clamped at -40 to 0 pA during drug wash-on experiments. We also calculated other
641 intrinsic electrophysiological parameters, such as the input resistance, membrane time constant,
642 spike amplitude, after-hyperpolarization (AHP) etc. (90–92).

643 **Plethysmography**

644 Plethysmography on conscious, unrestrained mice was carried out as described on 6-12 week
645 old adult animals (52,88). Mice were subjected to a five-day habituation protocol with each day
646 consisting of several minutes of handling, temperature taken by rectal probe, intraperitoneal saline
647 injection, and 30 minutes in the plethysmography chamber. Mice were then tested within one
648 week of the last day of conditioning.

649 On the day of testing, mice were taken from their home cage, weighed, and rectal temperature
650 was taken. Animals were then placed into an airtight, temperature controlled (~32°C)
651 plethysmography chamber and allowed to acclimate for at least 20 minutes in room air (21%
652 $O_2$/79% $N_2$) conditions. After acclimation and measurement under room air, the chamber gas was
653 switched to a hypercapnic mixture of 5% $CO_2$/21% $O_2$/74% $N_2$ for 20 minutes. Chamber gas was
654 then switched back to room air for 20 minutes. The mice were briefly removed for rectal
655 temperature measurement and intra-peritoneal injection of clozapine-N-oxide (CNO, National
656 Institute of Mental Health Chemical Synthesis and Drug Supply Program) dissolved in saline (0.1
657 mg/mL) for an effective concentration 1 mg/kg. The animal was returned to the chamber for
658 another 20 minutes of room air, 20 minutes of hypercapnia, and 20 minutes of room air. The
659 animal was then removed from the chamber and rectal temperature was taken immediately
660 afterwards and again 30 minutes after the termination of the experiment. The animal was placed
661 in its own cage during these 30 minutes at the ambient room temperature (~23°C).

662 ***Plethysmography data collection and analysis***

663 Plethysmography pressure changes were measured using a Validyne DP45 differential pressure
664 transducer and CD15 carrier demodulator in comparison to a reference chamber and recorded
665 with LabChartPro in real time. Waveforms were analyzed offline using LabChart Pro and custom
666 written MATLAB code (Supplemental Figure 3) to determine respiratory rate ($V_f$), tidal volume ($V_T$)

667 (52), minute ventilation ($\dot{V}_E$), oxygen consumption ($\dot{V}_{O2}$), ventilatory equivalents for oxygen
668 ($\dot{V}_E/\dot{V}_{O2}$), and pattern analysis. Respiratory waveforms were collected offline during periods when
669 the animal was at rest and readings were free from movement artifacts. A minimum of 1-minute
670 cumulative data compiled from traces at least 10 seconds long from the last 10 minutes of a given
671 experimental condition were analyzed. $O_2$ consumption was determined by comparing the gas
672 composition between calibration in an empty chamber and live breathing using an AEI oxygen
673 sensor and analyzer. Chamber temperature was constantly monitored and recorded using a
674 ThermoWorks MicroThermo 2 with probe and was recorded with LabChartPro in real time.

675 ***Plethysmography statistics***

676 Results ($V_f$, $V_T$, $\dot{V}_E$, $\dot{V}_{O2}$, $\dot{V}_E/\dot{V}_{O2}$) for room air and hypercapnic data were compared between all
677 cohorts using a linear mixed-effects regression model with animal type (experimental or control)
678 and CNO administration (pre- or post-injection) as fixed effects and animal ID as a random effect.
679 Temperature data was compared using a linear mixed-effects regression model with animal type
680 (experimental or control) as a fixed effect. Residuals were independent and identically distributed
681 as a normal distribution, which matches our model assumptions (Supplemental Figures 4-7). The
682 residual plot for ventilatory equivalents of oxygen in room air for hM4D (Fig. 8) shows a slightly
683 different distribution pattern (Supplemental Figure 5). However, this is because the random effect
684 coefficients are unusually small. This data still follows the normal and independent residuals
685 assumption. Random effect coefficient distribution is not as easily assessed with so few
686 datapoints and is not critical to statistical outcome if violated (93). The p-values reported
687 correspond to statistical significance of the conditional interaction between animal type and CNO
688 administration. A p-value of $<0.05$ was used to indicate statistical significance and standard error
689 of the mean is shown on all charts.

690 **Imaging of Twitch 2 in mouse preovulatory follicles**

691 Preovulatory follicles were isolated and imaged as previously described (94). Briefly, antral
692 follicles were dissected from 23- to 26-d-old *RR8; Bact_Cre mice*. Follicles were cultured for 24–
693 30 h on organotypic membranes (Millipore; cat. No. PICMORG50) in the presence of follicle-
694 stimulating hormone. The follicle was held in a perfusion slide consisting of a plastic slide (ibidi)
695 and a glass coverslip and assembled using silicon grease. The slide was constructed such that
696 medium containing ovine LH (National Hormone and Peptide Program; 10 µg/mL) could be
697 perfused through a 200-µm-deep channel holding the follicle. Temperature was maintained at
698 30–34 °C, by use of a warm air blower (Nevtek). Preovulatory Follicles were imaged using a Zeiss
699 Pascal confocal microscope with a 40X/1.2 NA objective. Images were collected every 10
700 seconds. Measurements were corrected for autofluorescence and for spectral bleed-through of
701 CFP into the YFP channel. Ratios were calculated by dividing the mean CFP intensity in each
702 region of interest by the mean YFP intensity. Data analysis was done using ImageJ and Excel
703 software. Data is representative of 4 follicles.

704 # Declarations

705 **Ethics approval and consent to participate**

706 All experiments reported herein were conducted with explicit approval of and oversight by both
707 Baylor College of Medicine Institutional Animal Care and Use Committee (IACUC) and University
708 of Connecticut IACUC and abide by all state and national regulations regarding animal research
709 for each work site.

710 **Consent for publication**

711 Not applicable.

712 **Availability of data and materials**

713 All datasets, animals, and materials generated and/ or used in this study are publicly available
714 (Addgene and Mutant Mouse Resource and Research Centers Supported by NIH (MMRRC)) or
715 available from the corresponding author on reasonable request.

716 **Competing interests**

717 The authors declare no competing interests.

718 **Funding**

719 R01: H1130249 (RR)

720 R21: OD025327 (RR)

721 R37: HD014939 (JRE and Laurinda A. Jaffe)

722 **Authors' contributions**

723 SJL completed experiments, analyzed data, and prepared the manuscript.

724 AM completed experiments, analyzed data, and prepared the manuscript.

725 PJH completed experiments, analyzed data, and prepared the manuscript.

726 PGF completed experiments, analyzed data and prepared the manuscript.

727 JP completed experiments, analyzed data, and prepared the manuscript.

728 AC completed statistical analyses and interpretations and prepared the manuscript.

729 JJS completed experiments, analyzed data, and prepared the manuscript.

730 VKM assisted in the completion of experiments.

731 PJZ completed experiments, analyzed data and prepared the manuscript

732 JRE completed experiments, analyzed data, and prepared the manuscript.

733 GA statistical analyses and interpretations and prepared the manuscript.

734 XJ completed experiments, analyzed data, and prepared the manuscript.

735 BRA completed experiments, analyzed data, and prepared the manuscript.

736 AST completed experiments, analyzed data and prepared the manuscript

737 M C-M assisted with experimental design and prepared the manuscript

738 RR conceptualized the study, performed experiments, analyzed data, and prepared the
739 manuscript.

740 All authors read and approved the final manuscript.

741 **Acknowledgements**

742 We thank M. Xue for providing the Cre and FLPo AAV viruses used in the dentate gyrus injection
743 and Ronda Kram for technical assistance with cloning, mouse husbandry, and maintenance. We
744 thank J. Dougherty, E. Schuman, J. Wess, B. Roth, and S. Sternson for providing plasmid
745 templates for the EGFP-L10A, MetRS, $G_s$-D, hM4D and hM3D, and PSAM cDNA, respectively.
746 We thank Laurinda A. Jaffe for collaborating with us and author JRE with the Twitch studies. The
747 Baylor College of Medicine Embryonic Stem (ES) Cell Core performed the ES cell
748 electroporations and were exceptionally helpful in our experiments and the Baylor College of
749 Medicine Genetically Engineered Mouse (GEM) Core performed the blastocyst injections.
750 Imaging was carried out at the Baylor College of Medicine Optical Imaging and Vital Microscopy
751 Core.

752 **Table 1. Publicly available modular targeting vectors for rapid generation of recombinase-**

753 **responsive ES cells and mouse lines.**

754 **Table 2. *Rosa26* knock-in alleles generated with or without CRISPR/Cas9 methods.** Shown
755 are targeted *Rosa26* alleles, function, length of cassette, current status, and expected MGI name
756 (to be determined) in grey rows.

757 **Table 3. Targeting efficiencies for a multiplexed five cassette ES cell electroporation for**

758 **the *Rosa26* locus.**

759 **Figure 1. Generation of intersectional *Rosa26* mouse lines**. **A)** Targeting schematic showing
760 the modular targeting vector containing a 1kb 5' homology arm, *CAG* promoter, *FRT*-flanked
761 neomycin and stop cassette, *LoxP*-flanked (optional) subtractive gene of interest (GOI-S) and
762 stop cassette, intersectional gene of interest (GOI-I), *WPRE*, *bgh poly A* element, and 1.2kb 3'
763 homology arm. The full intersectional cassette was knocked into the *Rosa26* locus, with a 22 bp
764 deletion of the CRISPR sgRNA. **B)** PCR genotyping of neomycin selected ES cell clones.
765 Targeting knock-in was determined using PCR primers that spanned from outside the *Rosa26*
766 homology arms to either the *CAG* promoter (5' end) or *WPRE* (3' end). Amplification of a band
767 indicates targeting. Shown are results from a targeting event with over 60% targeting efficiency
768 (*RR7*). **C)** Four conditions with different Cas9:targeting vector ratios were used in our initial study:
769 a 0:1 with no Cas9, 0.5:1, 1:1, and 10:1 **D)** Targeting efficiency results from the different ratios.
770 The 10:1 Cas9:targeting vector ratio showed a 5-10 fold increase over an electroporation with no
771 Cas9. Shown in red are results from previous electroporations using the traditional Rosa26
772 targeting vector with more commonly used longer homology arms.

773 **Figure 2. Analysis of *Rosa26* sgRNA off-target sites**. No mutations were seen in the top 5
774 potential off-target sites. **A)** List of top 10 potential off-target sites as determined by the Optimized
775 CRISPR tool, base pair mismatches, and location in the genome. **B-F)** Sequence chromatograms
776 of each off-target site, showing the correct sequence for each of the 3 selected clones that were
777 injected into blastocysts as compared to the wildtype sequence.

778 **Figure 3. Germline Cre/FLP expression in *RR5* adult mice to fluorescently label three**
779 **cellular compartments in targeted cells. A-H)** *RR5* mice bred to *DBH*$^{p2aFLP}$*; Bactin-Cre* mice
780 express Cre ubiquitously and FLP in all noradrenergic (NA) neurons, thus marking only NA
781 neurons, including the locus coeruleus (**A-D**) and A5 nucleus (**E-H**). **I-P)** *RR5* mice bred to
782 *Vgat_Cre; Vglut2-FLPo* mice with dual recombinase expression imaged in the entopeduncular
783 nucleus (**I-L**) and lateral habenula (**M-P**). In targeted cells that express both Cre and FLP, cell
784 nuclei are labeled with TagBFP, cell soma and processes are labeled with sfGFP, and pre-
785 synaptic contacts are labeled with tdTomato.

786 **Figure 4. Viral-mediated expression of Cre or FLP recombinase in *RR5* adult mice to**

787 **simultaneously, fluorescently label three cellular components.** *RR5* mice injected with

788 equal titers of AAV-Cre and AAV-FLP viruses into the dentate gyrus (**A-H**), basolateral

789 amygdala (**I-P**), and olfactory bulb (**Q-T**).

790 **Figure 5. Retrograde-viral Cre and germline FLP mediated expression of dual**
791 **recombinases for tricistronic FP expression on *RR5* background. A)** *RR5; DBH*$^{p2aFLPo}$ mice
792 were injected with CAV2-Cre virus into the basolateral amygdala. All *DBH* noradrenergic neurons
793 express FLP, but only those noradrenergic neurons projecting to the injected amygdala will also
794 express Cre. Marked double Cre/FLP positive cells will express H2B-TagBFP highlighting the
795 nucleus in blue, sfGFP filling the cell including the axon, and synaptophysin-tdTomato labeling
796 presynaptic contacts. BLA: Basolateral amygdala. DG: Dentate gyrus. DR: Dorsal raphé. LC:
797 Locus coeruleus. OB: Olfactory bulb. RtTg: Reticulotegmental pontine nucleus. *DBH* positive
798 neurons that project to the amygdala arise primarily from the ipsilateral locus coeruleus (**B-E**) with
799 some sparse labeling in the contralateral locus coeruleus (**F-I**). Red puncta overlapping with green
800 but lacking blue marked nuclei (indicative of projections from the marked population) can be seen
801 in a variety of mid- and forebrain areas, including the injected amygdala (**J-M**), the raphé nucleus
802 (**N-Q**), reticulotegmental pontine nuclei (**R-U**), dentate gyrus (**V-Y**), and olfactory bulb (**Z-CC**).

803 **Figure 6. Retrograde-viral FLP and germline Cre mediated expression of dual**
804 **recombinases for tricistronic FP expression on *RR5* background. A)** *RR5; Vglut2*$^{Cre}$ mice
805 were injected with retro-AAV-Ef1a-FLPo virus into the lateral hypothalamus. All *Vglut2* neurons
806 express Cre, but only those Vglut2 neurons projecting to the injected LHA will also express FLP.
807 Marked double Cre/FLP positive cells will express H2B-TagBFP highlighting the nucleus in blue,
808 sfGFP filling the cell including the axon, and synaptophysin-tdTomato labeling presynaptic
809 contacts. LHA: Lateral hypothalamic area. Vglut2 positive neurons that project to the LHA arise
810 from the cingulate gyrus (**B-E**), piriform cortex (**F-I**), and medial habenula (**J-M**).

811 **Figure 7. Electrophysiological characterization of CNO-DREADD mediated responses in**
812 **noradrenergic locus coeruleus (LC) neurons from lines *RR1(P), RR2(P),* and *RC::FPDi (P)*.**
813 **(A)** Representative wash-on responses of LC neurons from *RR1(P) (n=19*
814 *neurons), RR2(P) (n=10 neurons),* and *RC::FPDi*(P) *(n=10 neurons)* lines in response to
815 DREADD agonist CNO. **(B)** Membrane potentials of each LC neurons (pre-CNO vs post-CNO
816 values). **(C)** Summary plots of absolute voltage change for each DREADD line tested following
817 CNO treatment. (*$p<0.05$; **$p<0.01$).

818 **Figure 8. CNO-hM4D mediated perturbation of noradrenergic *DBH-Cre* neurons results in**
819 **a reduced hypercapnic response. A)** Representative breathing traces from a *DBH-Cre; RR1P*
820 animal before and after CNO administration under hypercapnic conditions
821 (5%$CO_2$/21%$O_2$/74%$N_2$). **B-F)** Quantification of respiratory and metabolic parameters under room
822 air and hypercapnic conditions in *DBH-Cre; RR1P* animals and sibling controls. Measured values
823 include respiratory rate (**B)**, tidal volume (**C)**, minute ventilation **(D)**, oxygen consumption **(E)**, and
824 minute ventilation normalized to oxygen consumption **(G)**. No difference was seen under room air
825 conditions but *DBH-Cre; RR1P* animals showed a deficit in volume, minute ventilation, and minute
826 ventilation normalized to oxygen consumption under hypercapnic conditions. **G)** No difference in
827 temperature was seen between *DBH-Cre; RR1P* animals and sibling controls. *$p<0.05$; **$p<0.01$;
828 ***$p<0.001$.

829 **Figure 9. CNO-hM3D mediated perturbation of noradrenergic *DBH-Cre* neurons results in**
830 **enhanced room air ventilation and a reduced hypercapnic response. A)** Representative
831 breathing traces from a *DBH-Cre; RR2P* animal before and after CNO administration under
832 room air conditions (21%$O_2$/79%$N_2$). **B)** Representative breathing traces from a *DBH-Cre;*
833 *RR2P* animal before and after CNO administration under hypercapnic conditions
834 (5%$CO_2$/21%$O_2$/74%$N_2$). **C-G)** Quantification of respiratory and metabolic parameters under
835 room air and hypercapnic conditions in *DBH-Cre; RR2P* animals and sibling controls. Measured
836 values include respiratory rate **(C)**, tidal volume **(D)**, minute ventilation **(E)**, oxygen consumption
837 **(F)**, and minute ventilation normalized to oxygen consumption **(G)**. After CNO administration,
838 *DBH-Cre; RR2P* animals showed increased rate, volume, minute ventilation, and oxygen
839 consumption under room air conditions. Under hypercapnic conditions, *DBH-Cre; RR2P* animals
840 showed increased oxygen consumption resulting in a reduced minute ventilation to oxygen
841 consumption value. **I)** *DBH-Cre; RR2P* animals showed a significant deficit in temperature 30
842 minutes after the end of the assay. *$p<0.05$; **$p<0.01$; ***$p<0.001$.

843 **Figure 10. Expression and function of Twitch-2B in the granulosa cells of mouse ovarian**
844 **follicles.** (**A**) A follicle from a mouse expressing Twitch-2B (homozygote). A follicle consists of
845 multiple layers of granulosa cells surrounding an oocyte in the center. Twitch-2B is uniformly
846 expressed in the granulosa cells but is not detectable in the oocyte. A layer of theca cells,
847 adhering to the outside of the follicle, expresses Twitch-2B at a higher level. Scale bar = 50 μm.
848 (**B**) ~6-fold increase in YFP/CFP ratio in the outer granulosa cells after application of 10 μM
849 ionomycin in the presence of 10 mM $CaCl_2$. Representative of 4 follicles.

850 **Supplemental Figure 1. Genetic schema for animals used to gather data for Figures 3-4.**

851 **Supplemental Figure 2. Genetic schema for animals used in Figures 7-9.**

852 **Supplemental Figure 3. Custom MatLab code for plethysmography data analysis.**

853 **Supplemental Table 4. QQplots for normal distribution testing of residuals from**

854 **plethysmography analyses from Fig. 8.**

855 **Supplemental Table 5. Residual plots for independence testing of residuals from**

856 **plethysmography analyses from Fig. 8.**

857 **Supplemental Table 6. QQplots for normal distribution testing of residuals from**

858 **plethysmography analyses from Fig. 9.**

859 **Supplemental Table 7. Residual plots for independence testing of residuals from**

860 **plethysmography analyses from Fig. 9.**

861 **REFERENCES**


862 1. Armbruster BN, Li X, Pausch MH, Herlitze S, Roth BL. Evolving the lock to fit the key to create a
863 family of G protein-coupled receptors potently activated by an inert ligand. Proc Natl Acad Sci
864 USA. 2007 Mar 20;104(12):5163–8.
865 2. Sauer B. Manipulation of transgenes by site-specific recombination: Use of Crerecombinase. Guide
866 to techniques in mouse development. Elsevier; 1993. p. 890–900.
867 3. Chuong AS, Miri ML, Busskamp V, Matthews GAC, Acker LC, Sørensen AT, et al. Noninvasive
868 optical inhibition with a red-shifted microbial rhodopsin. Nat Neurosci. 2014 Aug;17(8):1123–9.
869 4. Rowitch DH, S-Jacques B, Lee SM, Flax JD, Snyder EY, McMahon AP. Sonic hedgehog regulates
870 proliferation and inhibits differentiation of CNS precursor cells. J Neurosci. 1999 Oct
871 15;19(20):8954–65.
872 5. Urlinger S, Baron U, Thellmann M, Hasan MT, Bujard H, Hillen W. Exploring the sequence space
873 for tetracycline-dependent transcriptional activators: novel mutations yield expanded range and
874 sensitivity. Proc Natl Acad Sci USA. 2000 Jul 5;97(14):7963–8.
875 6. Sander JD, Joung JK. CRISPR-Cas systems for editing, regulating and targeting genomes. Nat
876 Biotechnol. 2014 Apr;32(4):347–55.
877 7. Platt RJ, Chen S, Zhou Y, Yim MJ, Swiech L, Kempton HR, et al. CRISPR-Cas9 knockin mice for
878 genome editing and cancer modeling. Cell. 2014 Oct 9;159(2):440–55.
879 8. Dubreuil V, Ramanantsoa N, Trochet D, Vaubourg V, Amiel J, Gallego J, et al. A human mutation
880 in Phox2b causes lack of CO2 chemosensitivity, fatal central apnea, and specific loss of parafacial
881 neurons. Proc Natl Acad Sci USA. 2008 Jan 22;105(3):1067–72.
882 9. Zucker SN, Bancroft TA, Place DE, Des Soye B, Bagati A, Berezney R. A dominant negative Cx43
883 mutant differentially affects tumorigenic and invasive properties in human metastatic melanoma
884 cells. J Cell Physiol. 2013 Apr;228(4):853–9.
885 10. LeMaster AM, Krimm RF, Davis BM, Noel T, Forbes ME, Johnson JE, et al. Overexpression of
886 brain-derived neurotrophic factor enhances sensory innervation and selectively increases neuron
887 number. J Neurosci. 1999 Jul 15;19(14):5919–31.
888 11. Collins AL, Levenson JM, Vilaythong AP, Richman R, Armstrong DL, Noebels JL, et al. Mild
889 overexpression of MeCP2 causes a progressive neurological disorder in mice. Hum Mol Genet.
890 2004 Nov 1;13(21):2679–89.
891 12. Ellis T, Smyth I, Riley E, Bowles J, Adolphe C, Rothnagel JA, et al. Overexpression of Sonic
892 Hedgehog suppresses embryonic hair follicle morphogenesis. Dev Biol. 2003 Nov 15;263(2):203–
893 15.
894 13. Ngo JT, Champion JA, Mahdavi A, Tanrikulu IC, Beatty KE, Connor RE, et al. Cell-selective
895 metabolic labeling of proteins. Nat Chem Biol. 2009 Oct;5(10):715–7.
896 14. Doyle JP, Dougherty JD, Heiman M, Schmidt EF, Stevens TR, Ma G, et al. Application of a
897 translational profiling approach for the comparative analysis of CNS cell types. Cell. 2008 Nov
898 14;135(4):749–62.
899 15. Marvin JS, Borghuis BG, Tian L, Cichon J, Harnett MT, Akerboom J, et al. An optimized
900 fluorescent probe for visualizing glutamate neurotransmission. Nat Methods. 2013 Feb;10(2):162–
901 70.
902 16. Akemann W, Mutoh H, Perron A, Park YK, Iwamoto Y, Knöpfel T. Imaging neural circuit
903 dynamics with a voltage-sensitive fluorescent protein. J Neurophysiol. 2012 Oct;108(8):2323–37.
904 17. Lin C-W, Sim S, Ainsworth A, Okada M, Kelsch W, Lois C. Genetically increased cell-intrinsic
905 excitability enhances neuronal integration into adult brain circuits. Neuron. 2010 Jan 14;65(1):32–
906 9.
907 18. Johns DC, Marx R, Mains RE, O'Rourke B, Marbán E. Inducible genetic suppression of neuronal
908 excitability. J Neurosci. 1999 Mar 1;19(5):1691–7.
909 19. Ibañez-Tallon I, Wen H, Miwa JM, Xing J, Tekinay AB, Ono F, et al. Tethering naturally occurring
910 peptide toxins for cell-autonomous modulation of ion channels and receptors in vivo. Neuron. 2004
911 Aug 5;43(3):305–11.

20. Duan B, Cheng L, Bourane S, Britz O, Padilla C, Garcia-Campmany L, et al. Identification of spinal circuits transmitting and gating mechanical pain. Cell. 2014 Dec 4;159(6):1417–32.
21. Kim JC, Cook MN, Carey MR, Shen C, Regehr WG, Dymecki SM. Linking genetically defined neurons to behavior through a broadly applicable silencing allele. Neuron. 2009 Aug 13;63(3):305–15.
22. Conklin BR, Hsiao EC, Claeysen S, Dumuis A, Srinivasan S, Forsayeth JR, et al. Engineering GPCR signaling pathways with RASSLs. Nat Methods. 2008 Aug;5(8):673–8.
23. Beier KT, Samson MES, Matsuda T, Cepko CL. Conditional expression of the TVA receptor allows clonal analysis of descendents from Cre-expressing progenitor cells. Dev Biol. 2011 May 15;353(2):309–20.
24. Magnus CJ, Lee PH, Atasoy D, Su HH, Looger LL, Sternson SM. Chemical and genetic engineering of selective ion channel-ligand interactions. Science. 2011 Sep 2;333(6047):1292–6.
25. Vardy E, Robinson JE, Li C, Olsen RHJ, DiBerto JF, Giguere PM, et al. A new DREADD facilitates the multiplexed chemogenetic interrogation of behavior. Neuron. 2015 May 20;86(4):936–46.
26. Zhao R, Grunke SD, Keralapurath MM, Yetman MJ, Lam A, Lee T-C, et al. Impaired Recall of Positional Memory following Chemogenetic Disruption of Place Field Stability. Cell Rep. 2016 Jul 19;16(3):793–804.
27. Beier KT, Saunders A, Oldenburg IA, Miyamichi K, Akhtar N, Luo L, et al. Anterograde or retrograde transsynaptic labeling of CNS neurons with vesicular stomatitis virus vectors. Proc Natl Acad Sci USA. 2011 Sep 13;108(37):15414–9.
28. Wickersham IR, Finke S, Conzelmann K-K, Callaway EM. Retrograde neuronal tracing with a deletion-mutant rabies virus. Nat Methods. 2007 Jan;4(1):47–9.
29. Zeisel A, Muñoz-Manchado AB, Codeluppi S, Lönnerberg P, La Manno G, Juréus A, et al. Brain structure. Cell types in the mouse cortex and hippocampus revealed by single-cell RNA-seq. Science. 2015 Mar 6;347(6226):1138–42.
30. Fuzik J, Zeisel A, Máté Z, Calvigioni D, Yanagawa Y, Szabó G, et al. Integration of electrophysiological recordings with single-cell RNA-seq data identifies neuronal subtypes. Nat Biotechnol. 2016 Feb;34(2):175–83.
31. Cadwell CR, Palasantza A, Jiang X, Berens P, Deng Q, Yilmaz M, et al. Electrophysiological, transcriptomic and morphologic profiling of single neurons using Patch-seq. Nat Biotechnol. 2016 Feb;34(2):199–203.
32. Awatramani R, Soriano P, Rodriguez C, Mai JJ, Dymecki SM. Cryptic boundaries in roof plate and choroid plexus identified by intersectional gene activation. Nat Genet. 2003 Sep;35(1):70–5.
33. Han X, Zhang Z, He L, Zhu H, Li Y, Pu W, et al. A suite of new Dre recombinase drivers markedly expands the ability to perform intersectional genetic targeting. Cell Stem Cell. 2021 Jun 3;28(6):1160–1176.e7.
34. Hirsch M-R, d'Autréaux F, Dymecki SM, Brunet J-F, Goridis C. A Phox2b::FLPo transgenic mouse line suitable for intersectional genetics. Genesis. 2013 Jul;51(7):506–14.
35. Dymecki SM, Ray RS, Kim JC. Mapping Cell Fate and Function Using Recombinase-Based Intersectional Strategies. Guide to Techniques in Mouse Development, Part B: Mouse Molecular Genetics, 2nd Edition. Elsevier; 2010. p. 183–213.
36. Robertson SD, Plummer NW, de Marchena J, Jensen P. Developmental origins of central norepinephrine neuron diversity. Nat Neurosci. 2013 Aug;16(8):1016–23.
37. Brust RD, Corcoran AE, Richerson GB, Nattie E, Dymecki SM. Functional and developmental identification of a molecular subtype of brain serotonergic neuron specialized to regulate breathing dynamics. Cell Rep. 2014 Dec 24;9(6):2152–65.
38. Niederkofler V, Asher TE, Okaty BW, Rood BD, Narayan A, Hwa LS, et al. Identification of Serotonergic Neuronal Modules that Affect Aggressive Behavior. Cell Rep. 2016 Nov 15;17(8):1934–49.
39. Ruffault P-L, D'Autréaux F, Hayes JA, Nomaksteinsky M, Autran S, Fujiyama T, et al. The

963 retrotrapezoid nucleus neurons expressing Atoh1 and Phox2b are essential for the respiratory
964 response to $CO_2$. Elife. 2015 Apr 13;4.
965 40. He M, Tucciarone J, Lee S, Nigro MJ, Kim Y, Levine JM, et al. Strategies and tools for
966 combinatorial targeting of gabaergic neurons in mouse cerebral cortex. Neuron. 2016 Sep
967 21;91(6):1228–43.
968 41. Madisen L, Garner AR, Shimaoka D, Chuong AS, Klapoetke NC, Li L, et al. Transgenic mice for
969 intersectional targeting of neural sensors and effectors with high specificity and performance.
970 Neuron. 2015 Mar 4;85(5):942–58.
971 42. Chen Y-W, Das M, Oyarzabal EA, Cheng Q, Plummer NW, Smith KG, et al. Genetic identification
972 of a population of noradrenergic neurons implicated in attenuation of stress-related responses. Mol
973 Psychiatry. 2019;24(5):710–25.
974 43. Tervo DGR, Hwang B-Y, Viswanathan S, Gaj T, Lavzin M, Ritola KD, et al. A designer AAV
975 variant permits efficient retrograde access to projection neurons. Neuron. 2016 Oct 19;92(2):372–
976 82.
977 44. Zingg B, Chou X-L, Zhang Z-G, Mesik L, Liang F, Tao HW, et al. AAV-Mediated Anterograde
978 Transsynaptic Tagging: Mapping Corticocollicular Input-Defined Neural Pathways for Defense
979 Behaviors. Neuron. 2017 Jan 4;93(1):33–47.
980 45. Kawano F, Okazaki R, Yazawa M, Sato M. A photoactivatable Cre-loxP recombination system for
981 optogenetic genome engineering. Nat Chem Biol. 2016 Dec;12(12):1059–64.
982 46. Tang JCY, Rudolph S, Dhande OS, Abraira VE, Choi S, Lapan SW, et al. Cell type-specific
983 manipulation with GFP-dependent Cre recombinase. Nat Neurosci. 2015 Sep;18(9):1334–41.
984 47. DeNardo LA, Liu CD, Allen WE, Adams EL, Friedmann D, Fu L, et al. Temporal evolution of
985 cortical ensembles promoting remote memory retrieval. Nat Neurosci. 2019 Jan 28;22(3):460–9.
986 48. Quadros RM, Miura H, Harms DW, Akatsuka H, Sato T, Aida T, et al. Easi-CRISPR: a robust
987 method for one-step generation of mice carrying conditional and insertion alleles using long
988 ssDNA donors and CRISPR ribonucleoproteins. Genome Biol. 2017 May 17;18(1):92.
989 49. Allen WE, Luo L. Intersectional illumination of neural circuit function. Neuron. 2015 Mar
990 4;85(5):889–92.
991 50. Zambrowicz BP, Imamoto A, Fiering S, Herzenberg LA, Kerr WG, Soriano P. Disruption of
992 overlapping transcripts in the ROSA beta geo 26 gene trap strain leads to widespread expression of
993 beta-galactosidase in mouse embryos and hematopoietic cells. Proc Natl Acad Sci USA. 1997 Apr
994 15;94(8):3789–94.
995 51. Soriano P. Generalized lacZ expression with the ROSA26 Cre reporter strain. Nat Genet. 1999
996 Jan;21(1):70–1.
997 52. Ray RS, Corcoran AE, Brust RD, Kim JC, Richerson GB, Nattie E, et al. Impaired respiratory and
998 body temperature control upon acute serotonergic neuron inhibition. Science. 2011 Jul
999 29;333(6042):637–42.
1000 53. Cong L, Ran FA, Cox D, Lin S, Barretto R, Habib N, et al. Multiplex genome engineering using
1001 CRISPR/Cas systems. Science. 2013 Feb 15;339(6121):819–23.
1002 54. Sun JJ, Ray R. Generation of Two Noradrenergic-Specific Dopamine-Beta-Hydroxylase-FLPo
1003 Knock-In Mice Using CRISPR/Cas9-Mediated Targeting in Embryonic Stem Cells. PLoS One.
1004 2016 Jul 21;11(7):e0159474.
1005 55. Thestrup T, Litzlbauer J, Bartholomäus I, Mues M, Russo L, Dana H, et al. Optimized ratiometric
1006 calcium sensors for functional in vivo imaging of neurons and T lymphocytes. Nat Methods. 2014
1007 Feb;11(2):175–82.
1008 56. Alexander GM, Rogan SC, Abbas AI, Armbruster BN, Pei Y, Allen JA, et al. Remote control of
1009 neuronal activity in transgenic mice expressing evolved G protein-coupled receptors. Neuron. 2009
1010 Jul 16;63(1):27–39.
1011 57. Guettier J-M, Gautam D, Scarselli M, Ruiz de Azua I, Li JH, Rosemond E, et al. A chemical-
1012 genetic approach to study G protein regulation of beta cell function in vivo. Proc Natl Acad Sci
1013 USA. 2009 Nov 10;106(45):19197–202.

1014 58. Heiman M, Kulicke R, Fenster RJ, Greengard P, Heintz N. Cell type-specific mRNA purification
1015 by translating ribosome affinity purification (TRAP). Nat Protoc. 2014 May 8;9(6):1282–91.
1016 59. Li L, Tasic B, Micheva KD, Ivanov VM, Spletter ML, Smith SJ, et al. Visualizing the distribution
1017 of synapses from individual neurons in the mouse brain. PLoS One. 2010 Jul 9;5(7):e11503.
1018 60. Root DH, Zhang S, Barker DJ, Miranda-Barrientos J, Liu B, Wang H-L, et al. Selective Brain
1019 Distribution and Distinctive Synaptic Architecture of Dual Glutamatergic-GABAergic Neurons.
1020 Cell Rep. 2018 Jun 19;23(12):3465–79.
1021 61. Shabel SJ, Proulx CD, Piriz J, Malinow R. Mood regulation. GABA/glutamate co-release controls
1022 habenula output and is modified by antidepressant treatment. Science. 2014 Sep
1023 19;345(6203):1494–8.
1024 62. Hnasko TS, Perez FA, Scouras AD, Stoll EA, Gale SD, Luquet S, et al. Cre recombinase-mediated
1025 restoration of nigrostriatal dopamine in dopamine-deficient mice reverses hypophagia and
1026 bradykinesia. Proc Natl Acad Sci USA. 2006 Jun 6;103(23):8858–63.
1027 63. Soudais C, Laplace-Builhe C, Kissa K, Kremer EJ. Preferential transduction of neurons by canine
1028 adenovirus vectors and their efficient retrograde transport in vivo. FASEB J. 2001
1029 Oct;15(12):2283–5.
1030 64. Plummer NW, Chandler DJ, Powell JM, Scappini EL, Waterhouse BD, Jensen P. An Intersectional
1031 Viral-Genetic Method for Fluorescent Tracing of Axon Collaterals Reveals Details of
1032 Noradrenergic Locus Coeruleus Structure. Eneuro. 2020 May 15;7(3).
1033 65. Rodríguez CI, Buchholz F, Galloway J, Sequerra R, Kasper J, Ayala R, et al. High-efficiency
1034 deleter mice show that FLPe is an alternative to Cre-loxP. Nat Genet. 2000 Jun;25(2):139–40.
1035 66. Bang SJ, Jensen P, Dymecki SM, Commons KG. Projections and interconnections of genetically
1036 defined serotonin neurons in mice. Eur J Neurosci. 2012 Jan;35(1):85–96.
1037 67. Egbert JR, Fahey PG, Reimer J, Owen CM, Evsikov AV, Nikolaev VO, et al. Follicle-stimulating
1038 hormone and luteinizing hormone increase Ca2+ in the granulosa cells of mouse ovarian follicles†.
1039 Biol Reprod. 2019 May 14;
1040 68. Quadros RM, Miura H, Harms DW, Akatsuka H, Sato T, Aida T, et al. Easi-CRISPR: a robust
1041 method for one-step generation of mice carrying conditional and insertion alleles using long
1042 ssDNA donors and CRISPR ribonucleoproteins. Genome Biol. 2017 May 17;18(1):92.
1043 69. Wang B, Li K, Wang A, Reiser M, Saunders T, Lockey RF, et al. Highly efficient CRISPR/HDR-
1044 mediated knock-in for mouse embryonic stem cells and zygotes. BioTechniques. 2015 Oct
1045 1;59(4):201–2, 204, 206.
1046 70. Chu VT, Weber T, Graf R, Sommermann T, Petsch K, Sack U, et al. Efficient generation of Rosa26
1047 knock-in mice using CRISPR/Cas9 in C57BL/6 zygotes. BMC Biotechnol. 2016 Jan 16;16:4.
1048 71. Yoshimi K, Kunihiro Y, Kaneko T, Nagahora H, Voigt B, Mashimo T. ssODN-mediated knock-in
1049 with CRISPR-Cas for large genomic regions in zygotes. Nat Commun. 2016 Jan 20;7:10431.
1050 72. Jensen P, Farago AF, Awatramani RB, Scott MM, Deneris ES, Dymecki SM. Redefining the
1051 serotonergic system by genetic lineage. Nat Neurosci. 2008 Apr;11(4):417–9.
1052 73. Bochkov YA, Palmenberg AC. Translational efficiency of EMCV IRES in bicistronic vectors is
1053 dependent upon IRES sequence and gene location. BioTechniques. 2006 Sep;41(3):283–4, 286,
1054 288 passim.
1055 74. Viemari J-C, Roux J-C, Tryba AK, Saywell V, Burnet H, Peña F, et al. Mecp2 deficiency disrupts
1056 norepinephrine and respiratory systems in mice. J Neurosci. 2005 Dec 14;25(50):11521–30.
1057 75. Viemari J-C, Ramirez J-M. Norepinephrine differentially modulates different types of respiratory
1058 pacemaker and nonpacemaker neurons. J Neurophysiol. 2006 Apr;95(4):2070–82.
1059 76. Li A, Emond L, Nattie E. Brainstem catecholaminergic neurons modulate both respiratory and
1060 cardiovascular function. Adv Exp Med Biol. 2008;605:371–6.
1061 77. Biancardi V, Bícego KC, Almeida MC, Gargaglioni LH. Locus coeruleus noradrenergic neurons
1062 and CO2 drive to breathing. Pflugers Arch. 2008 Mar;455(6):1119–28.
1063 78. Viemari J-C. Noradrenergic modulation of the respiratory neural network. Respir Physiol
1064 Neurobiol. 2008 Dec 10;164(1–2):123–30.

1065 79. Gargaglioni LH, Hartzler LK, Putnam RW. The locus coeruleus and central chemosensitivity.
1066 Respir Physiol Neurobiol. 2010 Oct 31;173(3):264–73.
1067 80. Kuo F-S, Falquetto B, Chen D, Oliveira LM, Takakura AC, Mulkey DK. In vitro characterization
1068 of noradrenergic modulation of chemosensitive neurons in the retrotrapezoid nucleus. J
1069 Neurophysiol. 2016 Sep 1;116(3):1024–35.
1070 81. Engelbrecht AH, Russell V, Carstens ME, De Villiers AS, Searson A, Jaffer A, et al. Evidence that
1071 noradrenergic neurons in the A1 and A2 nuclei are lesioned by low doses of 6-OHDA injected into
1072 the locus coeruleus. J Neurosci Methods. 1994 Apr;52(1):57–60.
1073 82. Massey CA, Iceman KE, Johansen SL, Wu Y, Harris MB, Richerson GB. Isoflurane abolishes
1074 spontaneous firing of serotonin neurons and masks their pH/$CO_2$ chemosensitivity. J Neurophysiol.
1075 2015 Apr 1;113(7):2879–88.
1076 83. Cooper KE, Jones DL, Pittman QJ, Veale WL. The effect of noradrenaline, injected into the
1077 hypothalamus, on thermoregulation in the cat. J Physiol (Lond). 1976 Sep;261(1):211–22.
1078 84. Handley SL, Spencer PS. thermoregulatory effects of intraventricular injection of noradrenaline in
1079 the mouse and the influence of ambient temperature. J Physiol (Lond). 1972 Jun;223(3):619–31.
1080 85. Guyenet PG, Bayliss DA. Neural control of breathing and CO2 homeostasis. Neuron. 2015 Sep
1081 2;87(5):946–61.
1082 86. Ray RS, Corcoran AE, Brust RD, Soriano LP, Nattie EE, Dymecki SM. Egr2-neurons control the
1083 adult respiratory response to hypercapnia. Brain Res. 2013 May 20;1511:115–25.
1084 87. Hennessy ML, Corcoran AE, Brust RD, Chang Y, Nattie EE, Dymecki SM. Activity of
1085 Tachykinin1-Expressing Pet1 Raphe Neurons Modulates the Respiratory Chemoreflex. J Neurosci.
1086 2017 Feb 15;37(7):1807–19.
1087 88. Martinez VK, Saldana-Morales F, Sun JJ, Zhu PJ, Costa-Mattioli M, Ray RS. Off-Target Effects of
1088 Clozapine-N-Oxide on the Chemosensory Reflex Are Masked by High Stress Levels. Front
1089 Physiol. 2019 May 22;10:521.
1090 89. Ting JT, Daigle TL, Chen Q, Feng G. Acute brain slice methods for adult and aging animals:
1091 application of targeted patch clamp analysis and optogenetics. Patch.
1092 90. Jiang X, Shen S, Cadwell CR, Berens P, Sinz F, Ecker AS, et al. Principles of connectivity among
1093 morphologically defined cell types in adult neocortex. Science. 2015 Nov 27;350(6264):aac9462.
1094 91. Scala F, Kobak D, Shan S, Bernaerts Y, Laturnus S, Cadwell CR, et al. Layer 4 of mouse neocortex
1095 differs in cell types and circuit organization between sensory areas. Nat Commun. 2019 Sep
1096 13;10(1):4174.
1097 92. Scala F, Kobak D, Bernabucci M, Bernaerts Y, Cadwell CR, Castro JR, et al. Phenotypic variation
1098 of transcriptomic cell types in mouse motor cortex. Nature. 2020 Nov 12;
1099 93. Schielzeth H, Dingemanse NJ, Nakagawa S, Westneat DF, Allegue H, Teplitsky C, et al.
1100 Robustness of linear mixed-effects models to violations of distributional assumptions. Methods
1101 Ecol Evol. 2020 Jun 12;
1102 94. Shuhaibar LC, Egbert JR, Norris RP, Lampe PD, Nikolaev VO, Thunemann M, et al. Intercellular
1103 signaling via cyclic GMP diffusion through gap junctions restarts meiosis in mouse ovarian
1104 follicles. Proc Natl Acad Sci USA. 2015 Apr 28;112(17):5527–32.
1105

# Figure 1

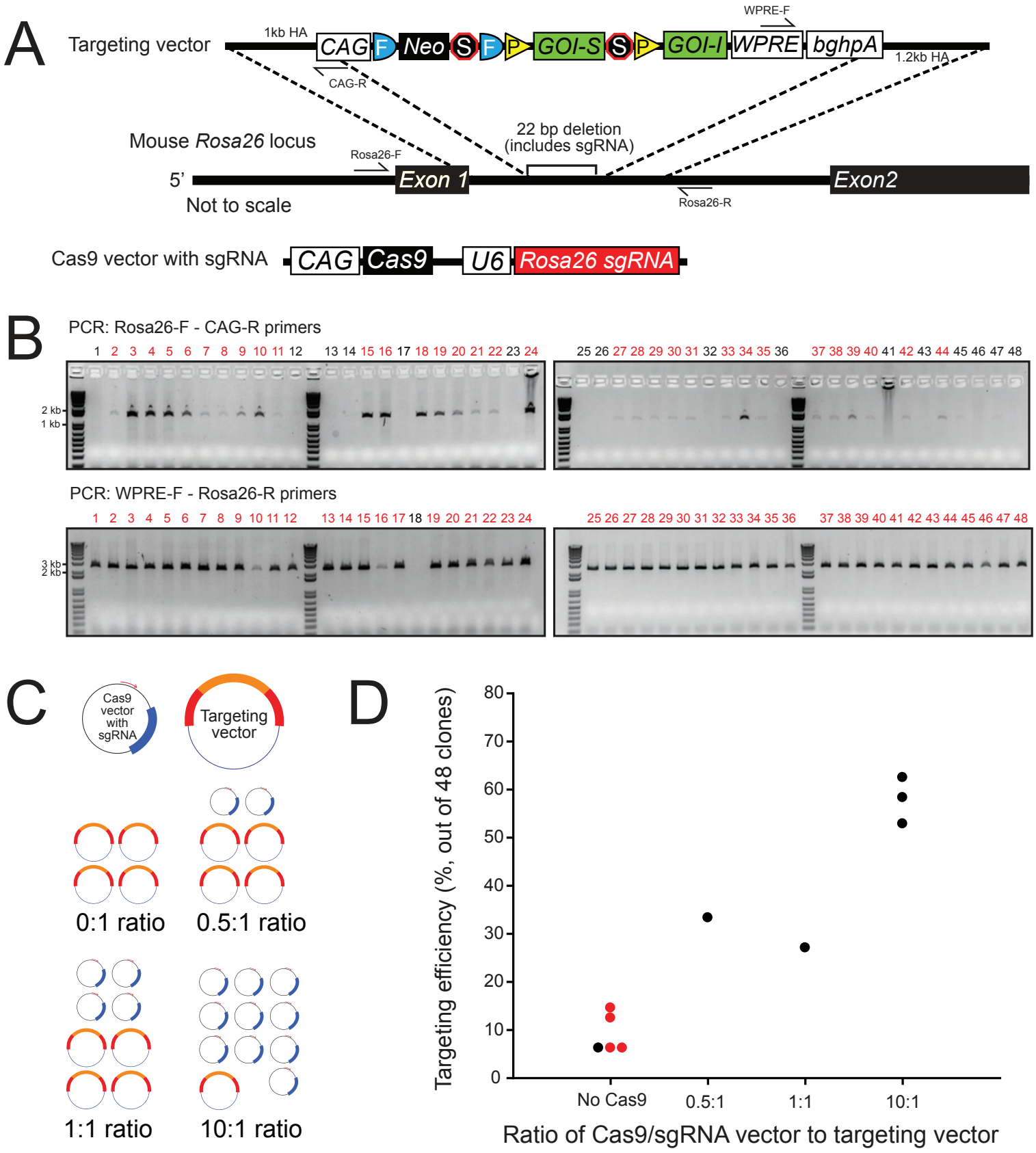
A
Targeting vector
1kb HA
CAG
F
Neo
S
F
P
GOI-S
S
P
GOI-I
WPRE
bghpA
WPRE-F
1.2kb HA
CAG-R
Mouse Rosa26 locus
22 bp deletion
(includes sgRNA)
Rosa26-F
5'
Exon 1
Exon2
Rosa26-R
Not to scale
Cas9 vector with sgRNA
CAG
Cas9
U6
Rosa26 sgRNA
B
PCR: Rosa26-F - CAG-R primers
2 kb
1 kb
PCR: WPRE-F - Rosa26-R primers
3 kb
2 kb
C
Cas9 vector with sgRNA
Targeting vector
0:1 ratio
0.5:1 ratio
1:1 ratio
10:1 ratio
D
Targeting efficiency (%, out of 48 clones)
No Cas9
0.5:1
1:1
10:1
Ratio of Cas9/sgRNA vector to targeting vector

# Figure 2

A

| | Sequence | | Score | Mut | Locus |
|---|---|---|---|---|---|
| | ACTGGAGTTGCAGATCACGA | GGG | | | |
| Off1: | .T.T.....A. | CA. | 1.1 | 3MM | chr15:-9941110 |
| Off2: | C...TG...T..... | T.. | 0.8 | 4MM | chr14:-25087434 |
| Off3: | C.....C.TG..... | TA. | 0.7 | 4MM | chr9:+122854629 |
| Off4: | .T..A....TT..... | .A. | 0.7 | 4MM | chr6:-97126315 |
| Off5: | TA..C.....T | AA. | 0.7 | 4MM | chr16:-4397663 |
| Off6: | .T.....G.....A. | AA. | 0.7 | 3MM | chr10:+35384261 |
| Off7: | .A..A..A.....T. | A.. | 0.5 | 4MM | chr11:-82755370 |
| Off8: | .....AT.C..... | AA. | 0.5 | 3MM | chr6:-124885038 |
| Off9: | ..G.T....T.....T. | T.. | 0.5 | 4MM | chr6:-41845311 |
| Off10: | .....C..C....A..... | CA. | 0.5 | 3MM | chr12:+103941450 |
| Off11: | C.....AC.....C... | ... | 0.4 | 4MM | chr13:+43290788 |
| Off12: | .G.....AA.....C... | T.. | 0.4 | 4MM | chr8:+95318409 |
| Off13: | ....CT.....A.. | .A. | 0.4 | 3MM | chr1:+11497683 |
| Off14: | .A..T...G.....A. | TA. | 0.3 | 4MM | chr12:+13635268 |
| Off15: | .A.A...G.....G.. | ... | 0.3 | 4MM | chr6:+41114906 |

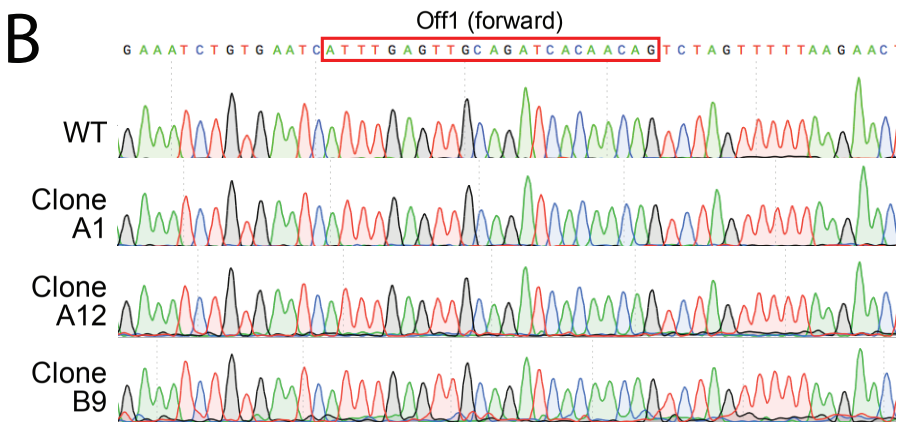


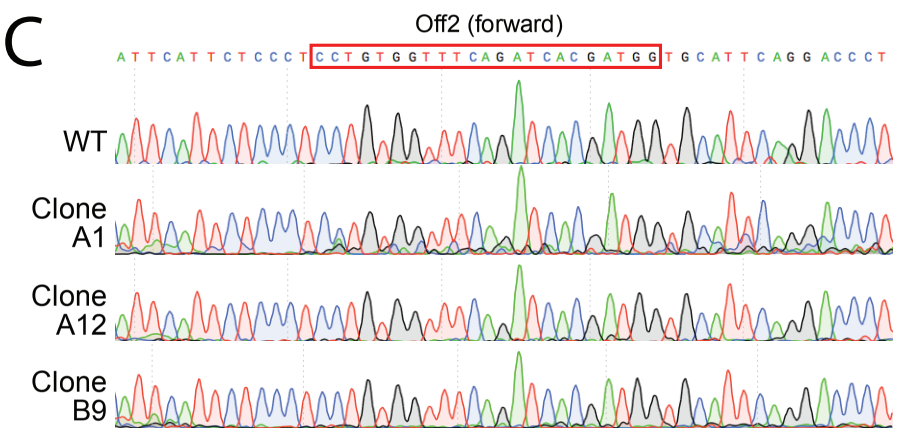


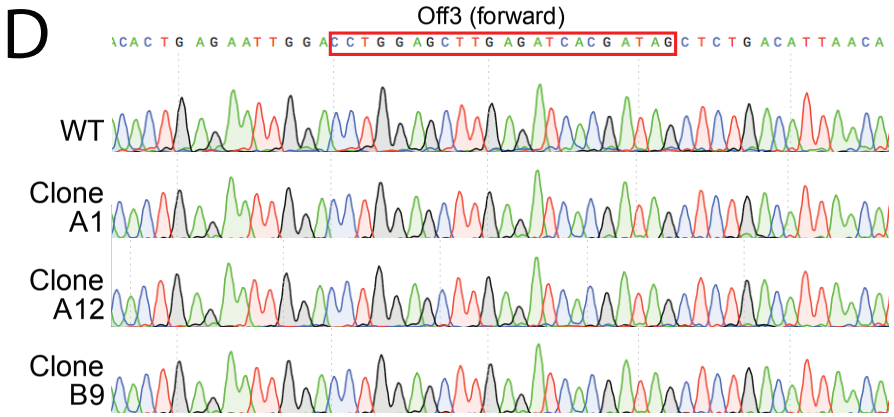


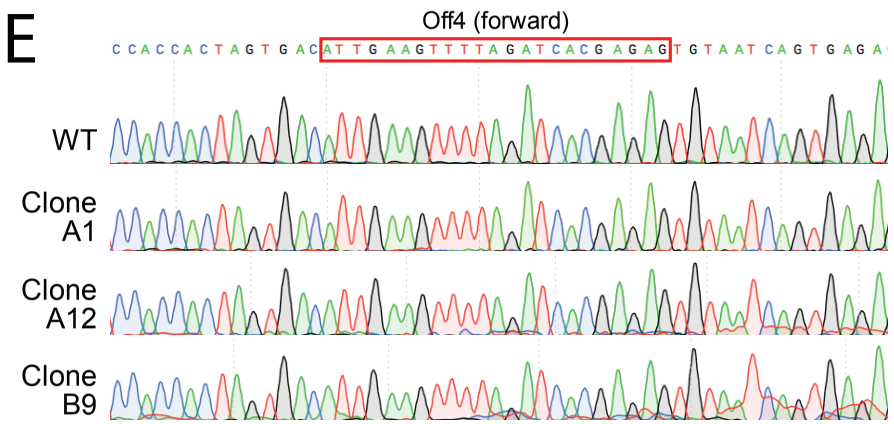


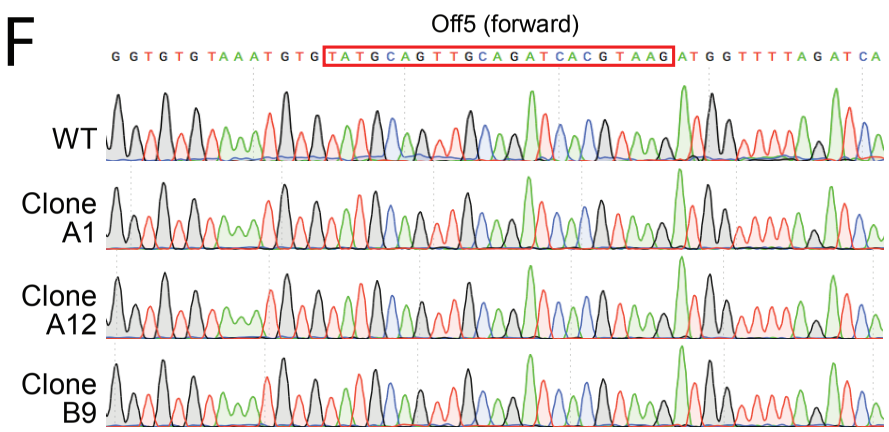

# Figure 3

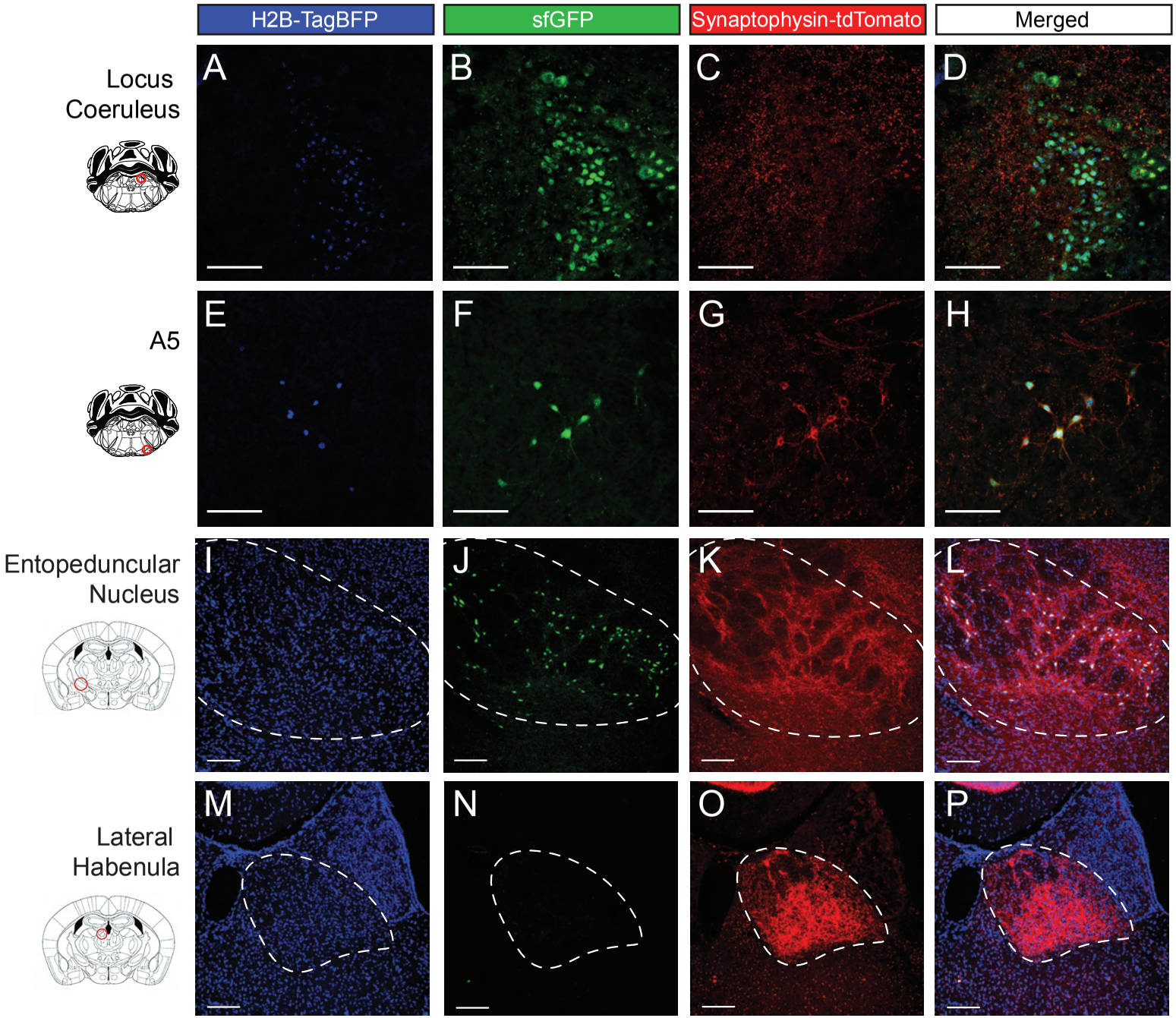
H2B-TagBFP
sfGFP
Synaptophysin-tdTomato
Merged
Locus Coeruleus
A5
Entopeduncular Nucleus
Lateral Habenula
A
B
C
D
E
F
G
H
I
J
K
L
M
N
O
P
Scale bar 50 μm

# Figure 4

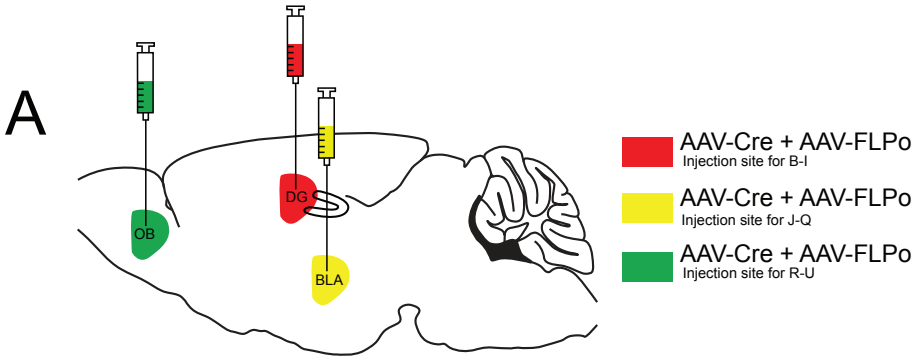


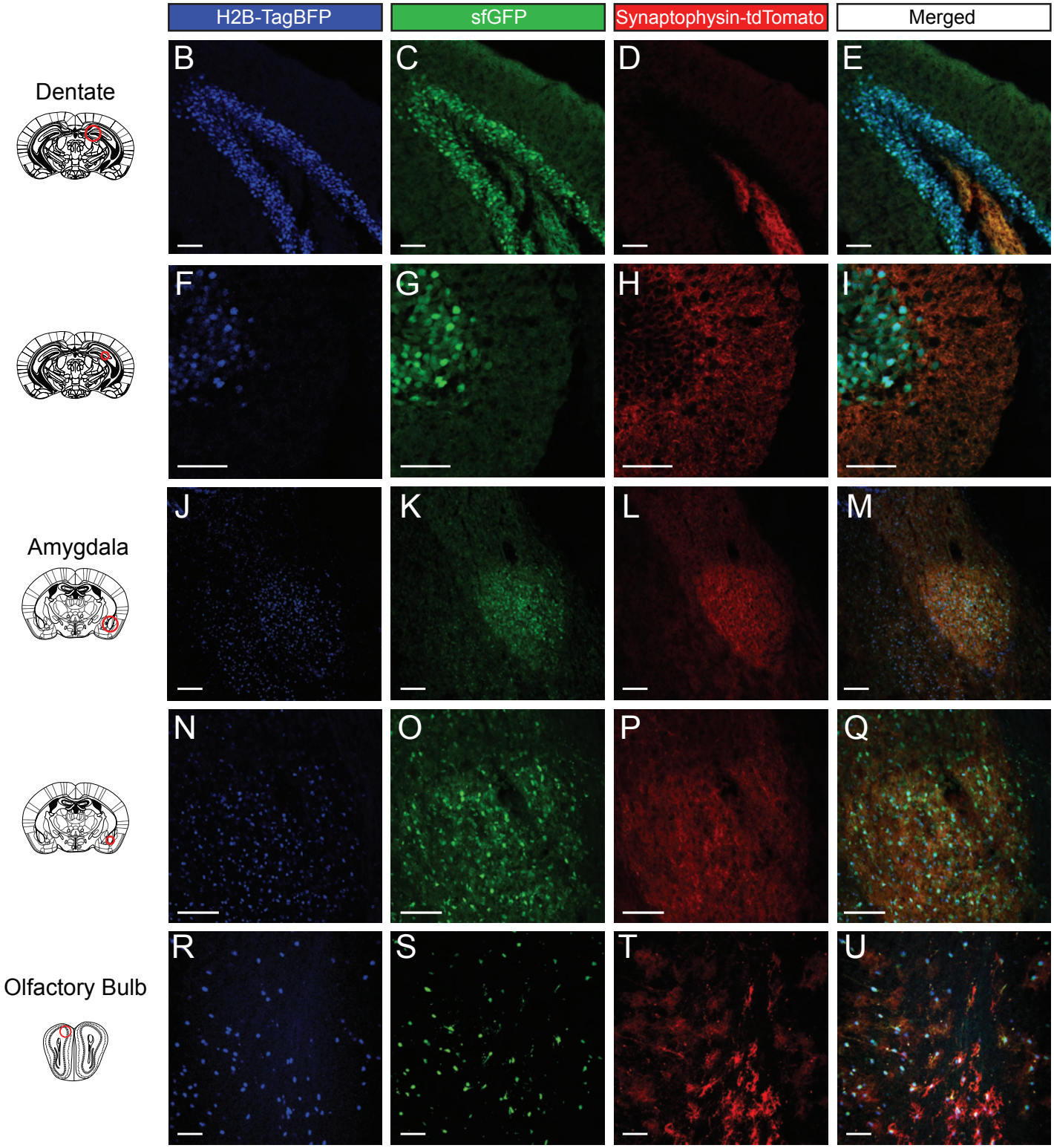


Scale bar 50 μm

# Figure 5

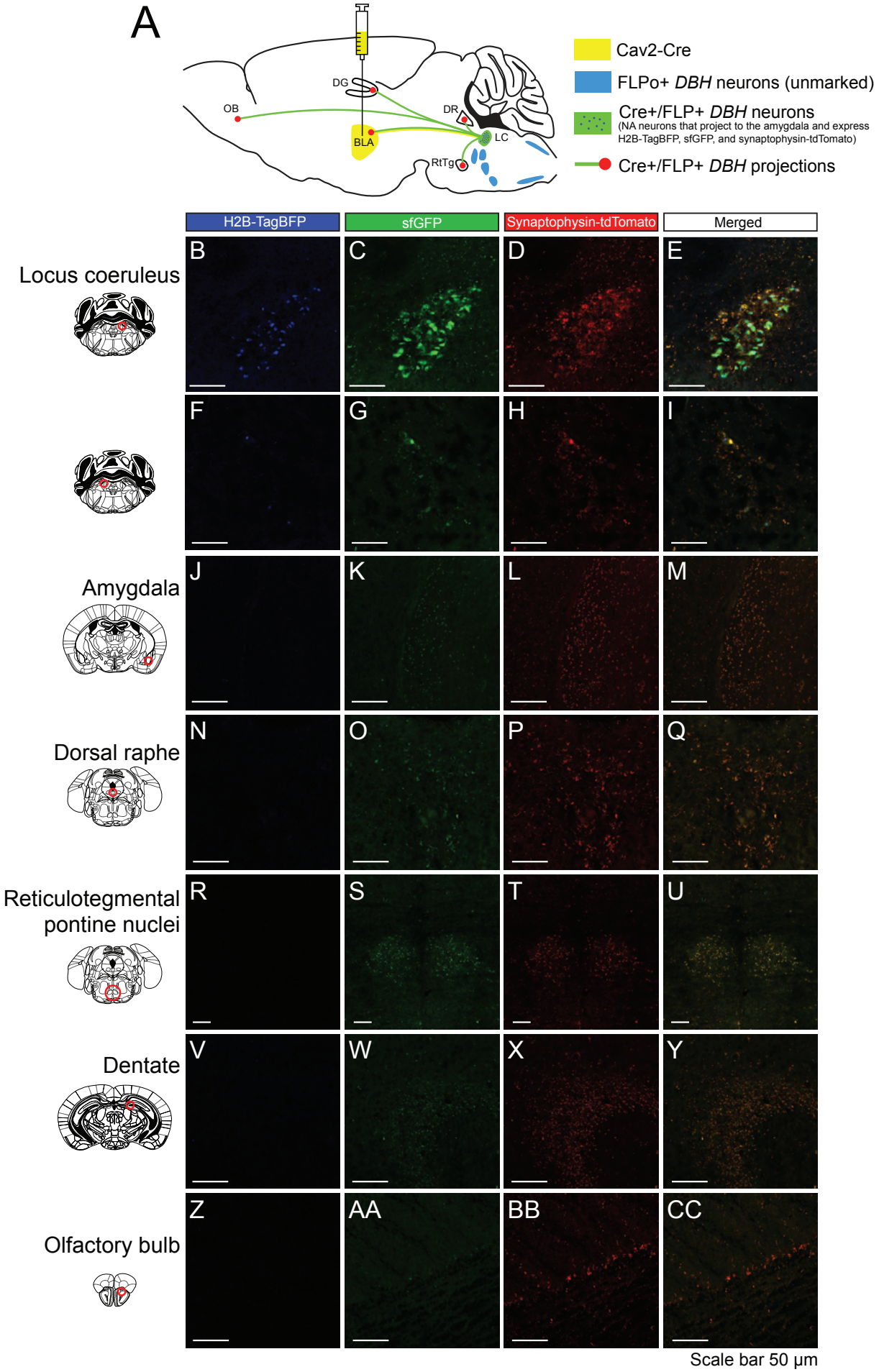
A
DG
OB
BLA
DR
LC
RtTg
Cav2-Cre
FLPo+ DBH neurons (unmarked)
Cre+/FLP+ DBH neurons
(NA neurons that project to the amygdala and express H2B-TagBFP, sfGFP, and synaptophysin-tdTomato)
Cre+/FLP+ DBH projections
H2B-TagBFP
sfGFP
Synaptophysin-tdTomato
Merged
Locus coeruleus
B
C
D
E
F
G
H
I
Amygdala
J
K
L
M
Dorsal raphe
N
O
P
Q
Reticulotegmental pontine nuclei
R
S
T
U
Dentate
V
W
X
Y
Olfactory bulb
Z
AA
BB
CC
Scale bar 50 μm

# Figure 6

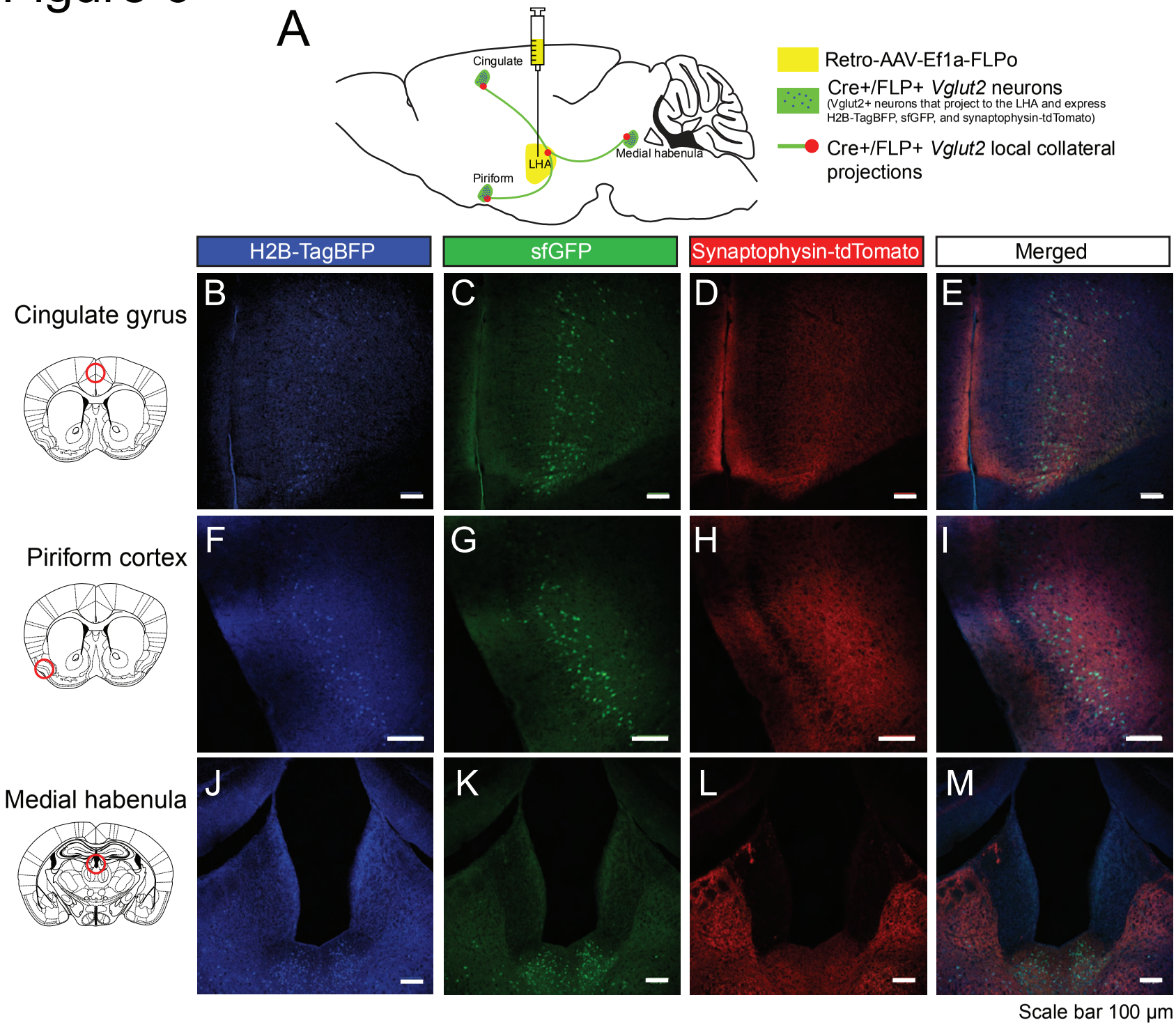
A
Cingulate
LHA
Medial habenula
Piriform
Retro-AAV-Ef1a-FLPo
Cre+/FLP+ Vglut2 neurons
(Vglut2+ neurons that project to the LHA and express H2B-TagBFP, sfGFP, and synaptophysin-tdTomato)
Cre+/FLP+ Vglut2 local collateral projections
H2B-TagBFP
sfGFP
Synaptophysin-tdTomato
Merged
Cingulate gyrus
Piriform cortex
Medial habenula
B
C
D
E
F
G
H
I
J
K
L
M
Scale bar 100 µm

# Figure 7

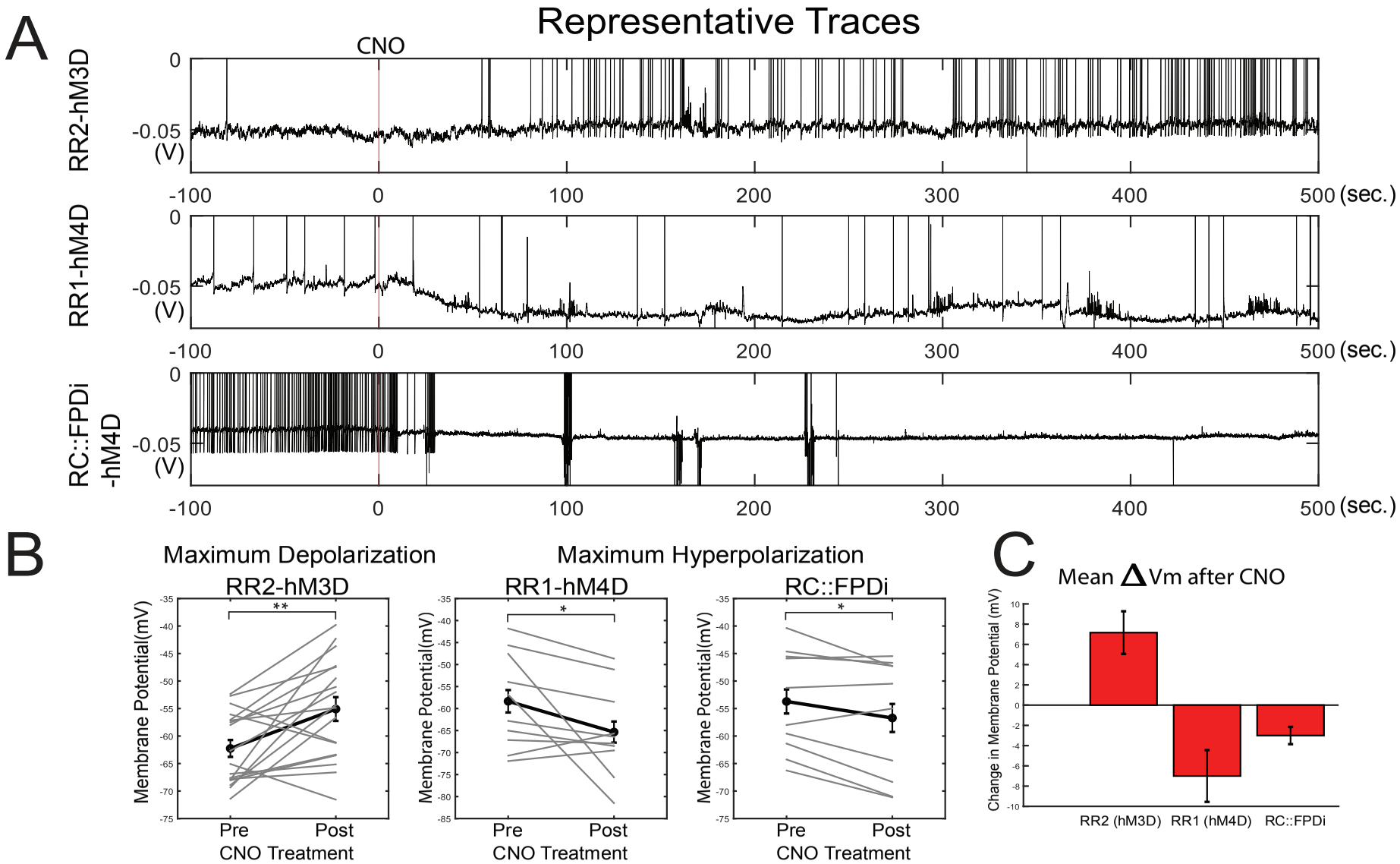
A
Representative Traces
CNO
RR2-hM3D
RR1-hM4D
RC::FPDi
-hM4D
0
-0.05
(V)
-100
0
100
200
300
400
500
(sec.)
B
Maximum Depolarization
Maximum Hyperpolarization
RR2-hM3D
RR1-hM4D
RC::FPDi
Membrane Potential(mV)
Pre
Post
CNO Treatment
**
*
C
Mean ΔVm after CNO
Change in Membrane Potential (mV)
RR2 (hM3D)
RR1 (hM4D)
RC::FPDi

# Figure 8

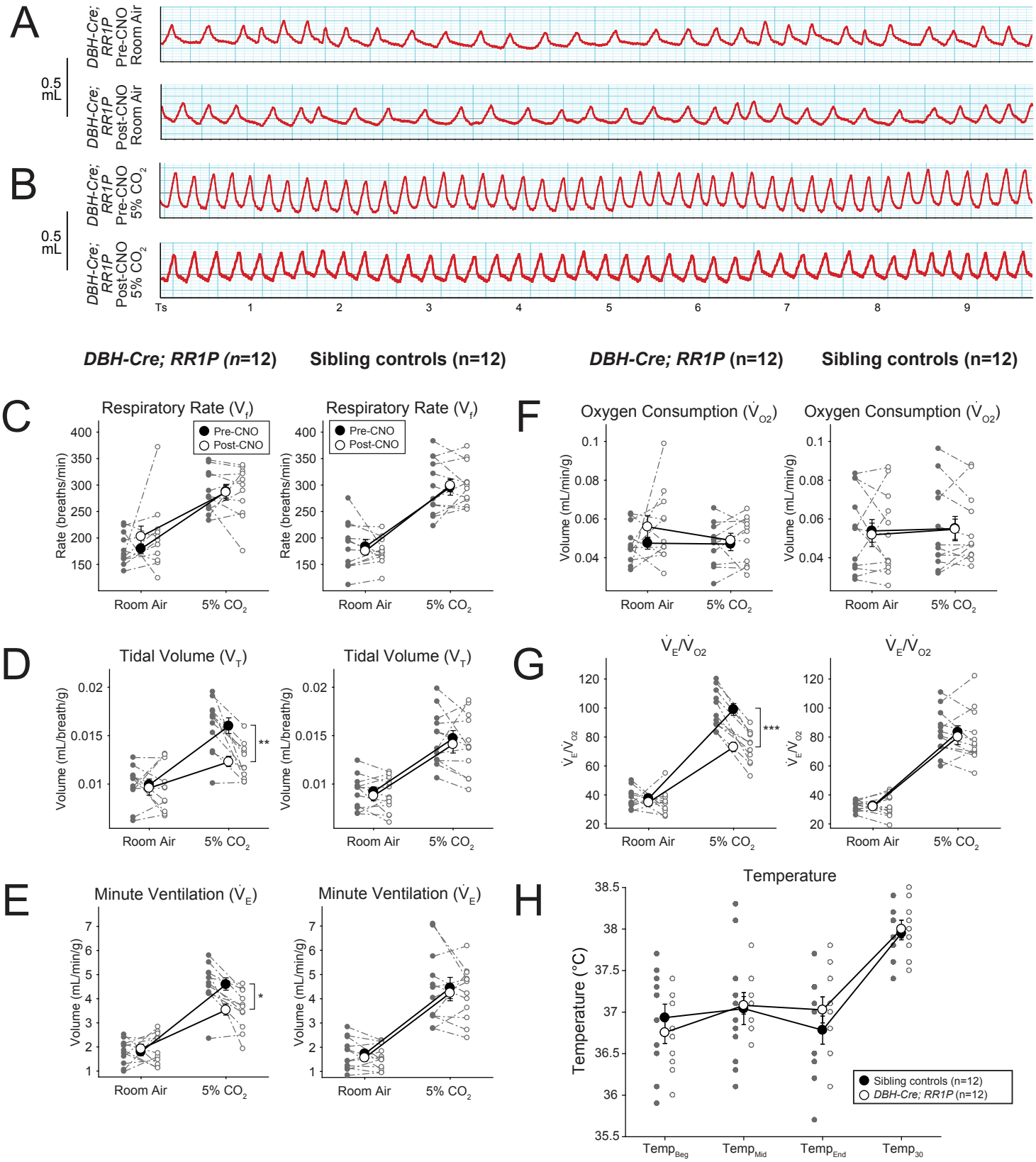
A
DBH-Cre; RR1P Pre-CNO Room Air
DBH-Cre; RR1P Post-CNO Room Air
0.5 mL
B
DBH-Cre; RR1P Pre-CNO 5% CO2
DBH-Cre; RR1P Post-CNO 5% CO2
0.5 mL
Ts 1 2 3 4 5 6 7 8 9
DBH-Cre; RR1P (n=12)
Sibling controls (n=12)
DBH-Cre; RR1P (n=12)
Sibling controls (n=12)
C
Respiratory Rate (Vf)
Pre-CNO
Post-CNO
Rate (breaths/min)
Room Air
5% CO2
D
Tidal Volume (VT)
Volume (mL/breath/g)
**
E
Minute Ventilation (V̇E)
Volume (mL/min/g)
*
F
Oxygen Consumption (V̇O2)
Volume (mL/min/g)
G
V̇E/V̇O2
***
H
Temperature
Temperature (°C)
Sibling controls (n=12)
DBH-Cre; RR1P (n=12)
TempBeg
TempMid
TempEnd
Temp30

# Figure 9

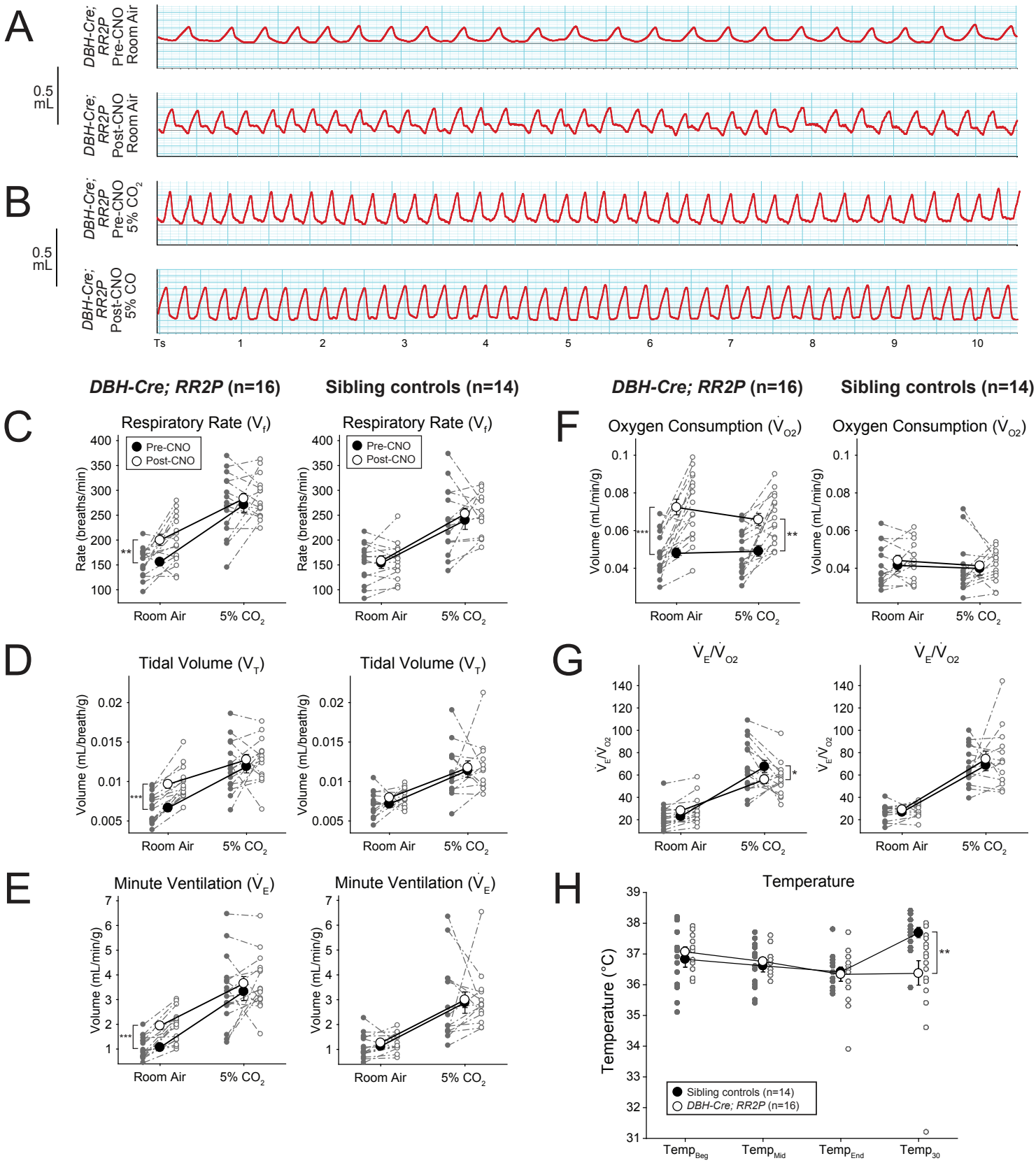
A
DBH-Cre; RR2P Pre-CNO Room Air
DBH-Cre; RR2P Post-CNO Room Air
0.5 mL
B
DBH-Cre; RR2P Pre-CNO 5% CO2
DBH-Cre; RR2P Post-CNO 5% CO
0.5 mL
Ts 1 2 3 4 5 6 7 8 9 10
DBH-Cre; RR2P (n=16)
Sibling controls (n=14)
C
Respiratory Rate (Vf)
Pre-CNO
Post-CNO
Rate (breaths/min)
Room Air
5% CO2
D
Tidal Volume (VT)
Volume (mL/breath/g)
E
Minute Ventilation (V̇E)
Volume (mL/min/g)
F
Oxygen Consumption (V̇O2)
Volume (mL/min/g)
G
V̇E/V̇O2
H
Temperature
Temperature (°C)
Sibling controls (n=14)
DBH-Cre; RR2P (n=16)
TempBeg
TempMid
TempEnd
Temp30

# Figure 10

A

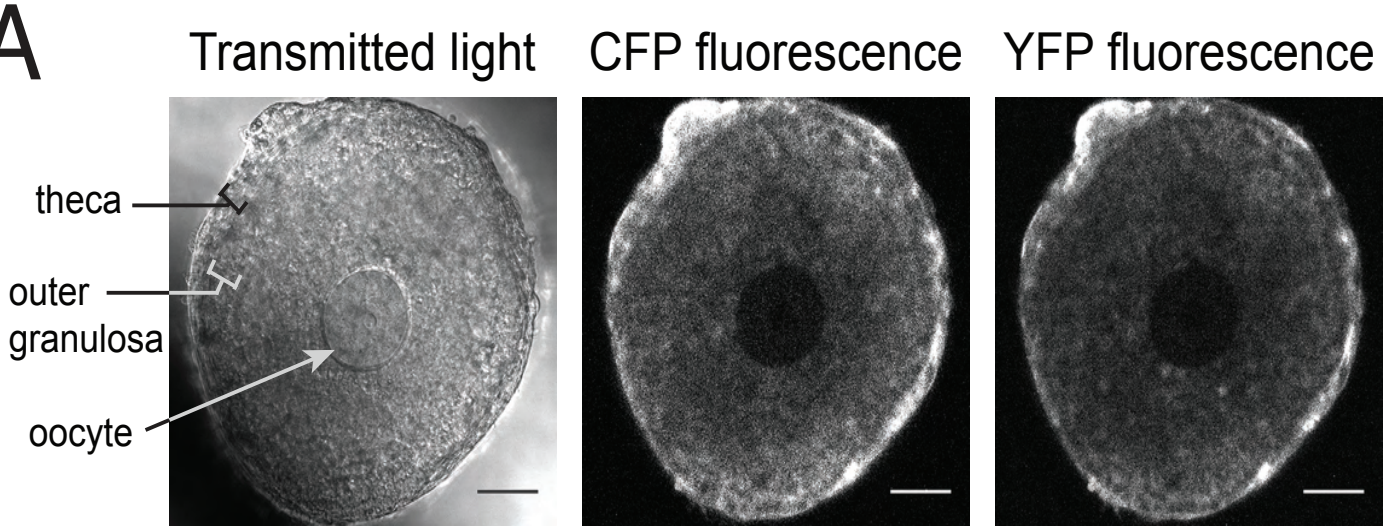
Transmitted light
CFP fluorescence
YFP fluorescence
theca
outer granulosa
oocyte

B

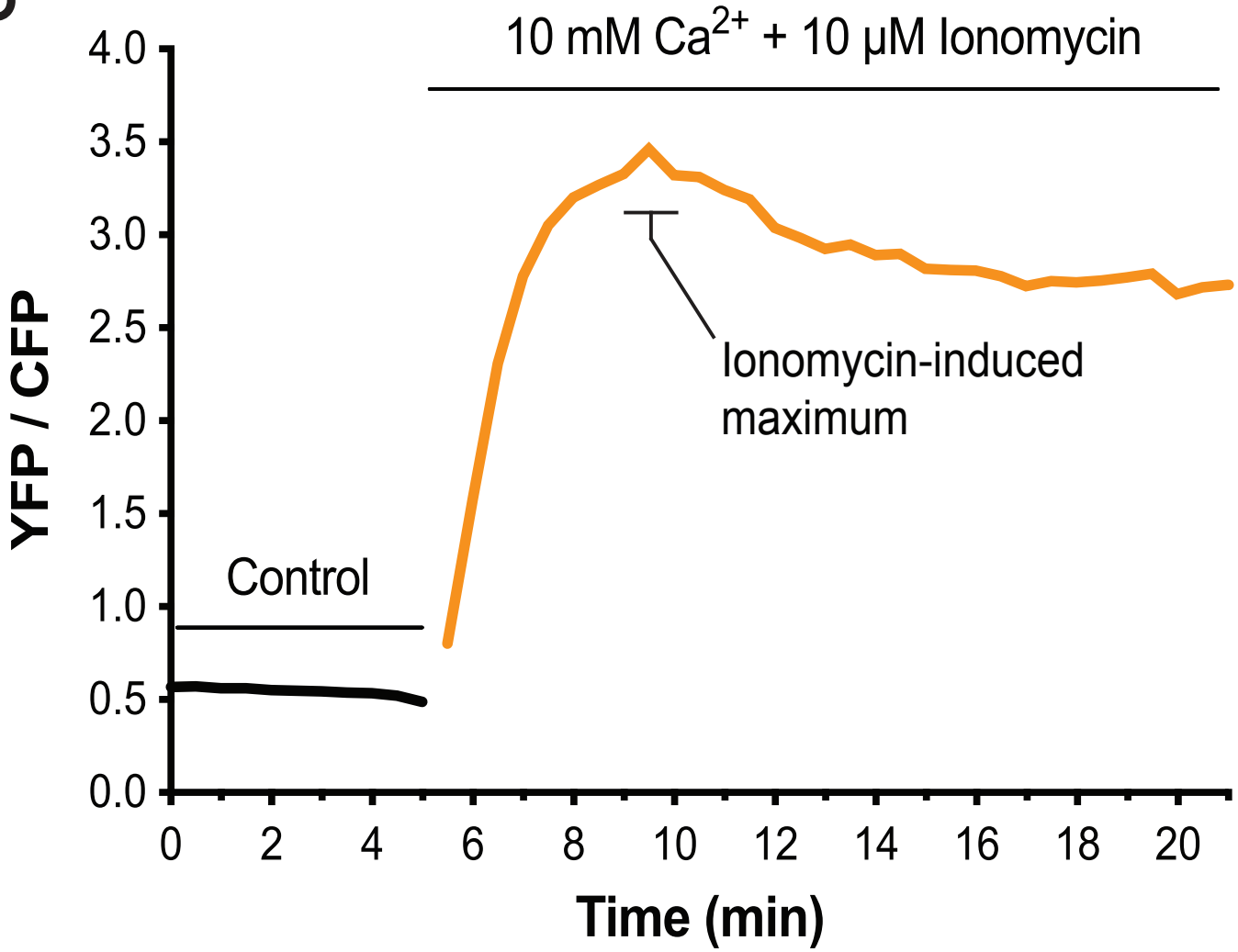
10 mM Ca2+ + 10 µM Ionomycin
Control
Ionomycin-induced maximum
YFP / CFP
4.0
3.5
3.0
2.5
2.0
1.5
1.0
0.5
0.0
0
2
4
6
8
10
12
14
16
18
20
Time (min)

# Table 1

| Vector | Function | Addgene ID Number |
|---|---|---|
| CAG Cas9 U6 Rosa26 sgRNA | Cas9 (px330) vector with sgRNA | 97007 |
| 5' homology arm CAG F Neo S F P CS S CS P 3' homology arm | FLP and Cre responsive cloning vector | 97012 |
| 5' homology arm CAG F S F P CS S CS P 3' homology arm | FLP and Cre responsive cloning vector (no neo) | 99142 |
| 5' homology arm CAG P Neo S P CS 3' homology arm | Cre responsive cloning vector | 97009 |
| 5' homology arm CAG F Neo S F CS 3' homology arm | FLP responsive cloning vector | 97010 |
| 5' homology arm CAG R Neo S R CS 3' homology arm | Dre responsive cloning vector | 97011 |
| 5' homology arm CS 3' homology arm | Empty *Rosa26* targeting vector | 97008 |

*CS: Cloning site

# Table 2

| Short Name | MMRRC ID | Subtractive gene | Intersectional gene | Function | Line status |
|---|---|---|---|---|---|
| *RR1** | 43516 | *mCherry* | *hM4D* | Metabotropic neuron perturbation | Established and functional |
| *Gt(ROSA)26Sor*$^{tm\#(CAG\text{-}mCherry,\text{-}hM4D)Rray}$ | | | | | |
| *RR2** | 43515 | *mCherry* | *hM3D* | Metabotropic neuron stimulation | Established and functional |
| *Gt(ROSA)26Sor*$^{tm\#(CAG\text{-}mCherry,\text{-}hM3D)Rray}$ | | | | | |
| *RR3** | 43518 | *mCherry* | *EGFP-L10A* | Translating mRNA pulldown | Established |
| *Gt(ROSA)26Sor*$^{tm\#(CAG\text{-}mCherry,\text{-}EGFP\text{-}L10A)Rray}$ | | | | | |
| *RR4** | 43519 | *mCherry* | *PSAM* | Ionotropic neuron perturbation | Established |
| *Gt(ROSA)26Sor*$^{tm\#(CAG\text{-}mCherry,\text{-}PSAM)Rray}$ | | | | | |
| *RR5* | 43513 | None | *H2B-TagBFP; sfGFP; synaptophysin-tdTomato* | Intersectional fluorescent marking | Established and functional |
| *Gt(ROSA)26Sor*$^{tm\#(CAG\text{-}H2B\text{-}TagBFP\text{-}sfGFP\text{-}synaptophysin\text{-}tdTomato)Rray}$ | | | | | |
| *RR6* | 43517 | *mCherry* | *Met-RS* | Synthesized protein pulldown | Established |
| *Gt(ROSA)26Sor*$^{tm\#(CAG\text{-}mCherry,\text{-}MetRS)Rray}$ | | | | | |
| *RR7* | 43514 | *mCherry* | *Rs-EGFP* | Metabotropic Gs excitation | Established |
| *Gt(ROSA)26Sor*$^{tm\#(CAG\text{-}mCherry,\text{-}Rs\text{-}eGFP)Rray}$ | | | | | |
| *RR8* | *TBD* | None | *Twitch2B* | Ratiometric calcium imaging | Established and functional |
| *Gt(ROSA)26Sor*$^{tm\#(CAG\text{-}Twitch2B)Rray}$ | | | | | |
| *RR9* | | *tdTomato* | *H2B-TagBFP; sfGFP* | Subtractive and intersectional fluorescent marking | Targeted ES cells |
| *Gt(ROSA)26Sor*$^{tm\#(CAG\text{-}tdTomato,\text{-}H2B\text{-}TagBFP\text{-}sfGFP)Rray}$ | | | | | |
| *RR10* | | None | *H2B-TagBFP; sfGFP* | Dre-responsive fluorescent marking | Targeted ES cells |
| *Gt(ROSA)26Sor*$^{tm\#(CAG\text{-}H2B\text{-}TagBFP\text{-}sfGFP)Rray}$ | | | | | |
| *RR11* | | None | *H2B-TagBFP; sfGFP; synaptophysin-tdTomato* | Dre-responsive fluorescent marking | Targeted ES cells |
| *Gt(ROSA)26Sor*$^{tm\#(CAG\text{-}H2B\text{-}TagBFP\text{-}sfGFP\text{-}synaptophysin\text{-}tdTomato)Rray}$ | | | | | |

Grey rows highlight Mouse Genome Informatics names; (tm#) are currently being determined
*Made using an earlier Rosa26 targeting vector without CRISPR/Cas9

# Table 3

| RR1-4 ES cell targeting vectors without Cas9 | | | |
|---|---|---|---|
| **Knock-in Cassette** | **Short name** | **Length** | **Efficiency** |
| CAG F S F P mCherry S P hM4D | *RR1* | 9312 bps | 6/48 (13%) |
| CAG F S F P mCherry S P hM3D | *RR2* | 9328 bps | 3/48 (6%) |
| CAG F S F P tdTomato S P EGFP-L10A | *RR3* | 9006 bps | 7/48 (14%) |
| CAG F S F P tdTomato S P PSAM | *RR4* | 8790 bps | 3/48 (6%) |

| RR5 -ES cell Cas9 co-electroporation knock-in efficiencies. | | |
|---|---|---|
| **RR5 Knock-in Cassette (12641 bp)** | **Cas9:Vector** | **Efficiency** |
| CAG F S F P S P H2B-TagBFP sfGFP synaptophysin-tdTomato | 0:1 | 3/48 (6%) |
| CAG F S F P S P H2B-TagBFP sfGFP synaptophysin-tdTomato | 0.5:1 | 16/48 (33%) |
| CAG F S F P S P H2B-TagBFP sfGFP synaptophysin-tdTomato | 1:1 | 13/48 (27%) |
| CAG F S F P S P H2B-TagBFP sfGFP synaptophysin-tdTomato | 10:1 | 28/48 (58%) |

| Multiplex ES cell cas9 knock-in efficiencies (Cas9 : Vector = 10.:1) | | | |
|---|---|---|---|
| **Knock-in Cassette** | **Short name** | **Length** | **Efficiency** |
| CAG F S F P mCherry S P Met-RS | *RR6* | 11037 bps | 6/48 (13%) |
| CAG F S F P mCherry S P Rs-EGFP | *RR7* | 9534 bps | 1/48 (2%) |
| CAG F S F P tdTomato S P H2B-TagBFP sfGFP | *RR9* | 9597 bps | 6/48 (13%) |
| CAG R S R H2B-TagBFP sfGFP synaptophysin-tdTomato | *RR11* | 9202 bps | 5/48 (10%) |
| CAG R S R H2B-TagBFP sfGFP | *RR10* | 6732 bps | 9/48 (19%) |
| | | **Multiplex vector electroporation total** | 25/48 (52%) |

| Oocyte cas9 knock-in efficiencies | | | |
|---|---|---|---|
| CAG P S P Twitch 2B | *RR8* | 6508 bps | 1/1266 (<1%) |